CORROSION AND STRESS CORROSION CRACK INITIATION OF COLD-WORKED ALLOY 690 IN PWR PRIMARY WATER

Technical Milestone Report: M2LW-13OR0402035
September 2013

M. B. Toloczko, M. J. Olszta, D. K. Schreiber
and S. M. Bruemmer
Pacific Northwest National Laboratory

Research Project:
Stress Corrosion Crack Initiation of
Nickel-Base Alloys in LWR Environments
Project Manager: S. M. Bruemmer
Pacific Northwest National Laboratory

Conducted for:
Office of Nuclear Energy, U.S. Department of Energy
Light Water Reactor Sustainability Program
Materials Aging and Degradation Pathway
Pathway Manager: J. T. Busby
Oak Ridge National Laboratory

Table of Contents

Project Background

Objective

This research project addresses one of the least understood aspects of stress corrosion cracking (SCC) for light-water reactor (LWR) pressure boundary components - crack initiation. The focus of the work is to investigate important material (composition, processing, microstructure) and environmental (water chemistry, temperature, electrochemical potential, stress) effects on the SCC susceptibility of corrosion-resistant nickel-base alloys. Primary objectives are to identify mechanisms controlling crack nucleation in these alloys under realistic LWR conditions and help establish the framework to effectively model and mitigate SCC initiation processes.

Approach

Alloy 600 materials were selected for the first phase of SCC initiation experimentation followed by testing on the more resistant alloy 690 materials. For both alloys, material variants known to influence SCC response are being examined including cold work (forged, rolled and tensile strained), banded/inhomogeneous microstructures (plate versus extruded pipe), grain boundary precipitation (heat-to-heat variations and changes due to thermal treatments) and surface grinding (various depths of damage). Materials and material conditions have been identified and obtained from ongoing research projects where stress-corrosion crack growth has been characterized, thus creating an important link between SCC initiation and propagation behavior. Detailed examinations are performed using optical and electron microscopy to establish key bulk and surface microstructural features that may act as initiation precursors. Dedicated test systems with continuous in-situ detection of crack formation have been designed and constructed enabling SCC initiation experimentation of a range of alloy 600 and 690 materials. After SCC testing in high temperature autoclave systems, surface and near-surface characterizations are conducted to document nano-to-microscale initiation precursors leading to macroscopic stress corrosion cracks. The fundamental understanding of how the near-surface microstructure is degraded during high-temperature water exposure is essential to an improved predictive methodology.

Focus of Current Report

This report reviews recent corrosion and preliminary SCC initiation testing on cold-worked alloy 690 materials in high-temperature, simulated PWR primary water. Scanning electron microscopy (SEM), transmission electron microscopy (TEM) and atom probe tomography (APT) were used extensively for the characterization of material and corrosion microstructures. The APT work in particular was possible through collaborative activities with DOE Office of Basic Energy Sciences (BES), Division of Materials Science & Engineering and the EMSL user facility at PNNL. Stress corrosion crack growth measurements have been performed, and SCC susceptibility established, on the cold-worked alloy 690 heats conducted as part of an ongoing project for the Nuclear Regulatory Commission at PNNL.

Experimental Details

Alloy 690 Materials Information and Specimens

Three commercial alloy 690 heats were chosen for characterization and crack initiation testing: an extruded control-rod-drive-mechanism (CRDM) heat RE243 from Valinox and two plate heats, NX3297HK12 received from Argonne National Laboratory (ANL) and B25K received from General Electric Global Research (GE). Bulk compositions, material conditions and microstructural information on these three heats are summarized in Tables 1 and 2. A more detailed explanation of the commercial alloys can be found elsewhere [1,2] along with a summary of their SCC response.

As part of surface characterization activities, the CRDM alloy 690TT material was exposed and examined in both the as-received and cold-rolled (CR) conditions, while the plate alloys were only studied in the CR condition. In addition, a high-purity Ni-30Cr binary alloy was also chosen for analysis in a high-temperature annealed condition. Information on this heat is also summarized in Tables 1 and 2.

Table 1. Alloy 690 Materials and Ni-30Cr High-Purity Model Alloy

Material and Heat Number	Description	Composition, wt%	Heat Treatments
PNNL Alloy 690TT RE243	Valinox CRDM Tube 2360 (1.4" wall)	Ni-28.9Cr-10.4Fe-0.02C-0.3Mn-0.35Si-0.14Al-0.23Ti-0.024N-0.008P-0.0005S	1122°C/~1 min, WQ + 716-725°C/10.5 h, air cool
ANL Alloy 690MA NX3297HK12	ATI Wah Chang 2.125" Plate	Ni-30.8Cr-8.5Fe-0.04C-0.33Mn-0.02Si-0.18Al-0.27Ti-0.037N-0.0006S-0.006P	1038°C/2 h, air cool (MIL-DTL-24802)
GE Alloy 690MA B25K	ATI Allvac 3.25" Plate	Ni-29.3Cr-9.2Fe-0.034C-0.22Mn-0.06Si-0.26Al-0.37Ti-0.026N-0.006P-<0.0003S	996°C/0.33 h, air cool
Ni-30Cr	Hot forged 60-mm square block	High Purity (Ni - 30 at% Cr) Ni-26.6Cr	950°C/1 h, air cool

Table 2. Microstructure for Alloy 690 Materials and Ni-30Cr High-Purity Model Alloy

Sample	Microstructure
PNNL CRDM Alloy 690TT	Semi-continuous (discrete + cellular) IG carbides, few IG and matrix TiN; equiaxed grains; grain boundary Cr depletion to ~21 wt%
PNNL CRDM 31%CR Alloy 690TT	Same as above, but with slightly elongated grains
GEG Plate 20%CR Alloy 690MA	Well-spaced IG carbides, higher density in banded areas, IG and matrix TiN, slightly elongated grains; no grain boundary Cr depletion
ANL Plate 26%CR Alloy 690MA	Semi-continuous IG carbides, IG and matrix TiN, no banding in SCC plane, slightly elongated grains; grain boundary Cr depletion to ~22 wt%
Ni-30Cr	Equiaxed grains, no second-phase precipitates, no grain boundary Cr depletion

A key goal for this program is to be able to correlate the SCC initiation time to various aspects of materials processing including bulk microstructure, near surface microstructure, surface texture, gross surface defects and stress level. Prior experience with alloys 600 and 690 has shown that their SCC crack growth resistance is extremely sensitive to the degree of plastic deformation, and therefore being able to accurately characterize it in the test specimen was an important factor in the selection of specimen type. Several different specimen types were considered for the crack initiation testing including U-bend, blunt notch compact tension (CT) and tensile geometries.

Ultimately, a tensile specimen geometry was the most attractive because it has none of the shortcomings associated with U-bend and blunt notch specimens. This design produces a uniaxial stress state, the gauge length is easily accessible allowing control over the surface microstructure, various types of defects can be easily generated, there are several ways to produce specimens with well known amounts of uniform plastic strain, and prior work at KAPL shown that DCPD can be effectively used to detect crack initiation [3].

Several factors played into the specific design of the tensile specimens employed for SCC initiation testing, however the most important of which was maximizing the ability of DCPD to detect crack initiation. One practical issue was that an initiation specimen should have dimensions that fit within the dimensions of a 0.5T CT specimen so that any material prepared for SCC crack growth studies could also be used for SCC crack initiation studies. The final tensile design was refined to the point that a crack initiation specimen can be cut from an SCC-tested 0.5T CT specimen as long the crack length a/W value does not exceed 0.7. This a/W is below the range of typical crack lengths in SCC studies conducted by PNNL allowing routine extraction of crack initiation specimens as desired. Other factors that went into the design were a need to electrically isolate the specimen and eliminate any significant stress risers. A photograph of the final design is shown in Figure 1. For phase 1 crack initiation testing, the gauge section surface finish was carefully prepared either to fine polish (1 μm finish) or a ground surface with the near-surface damage controlled by the media employed. A more detailed description of the corrosion and SCC test systems are provided in the following section.

Dedicated specimens for surface oxidation studies were fashioned into small, rectangular coupons (30 mm x 20 mm), of which one face was mechanically polished to a colloidal silica finish (~100 nm diameter particles). The amount of surface damage remaining was evaluated in cross-section specimens using low kV, SEM backscatter electron (BSE) imaging and determined to be negligible, as the bulk grain contrast was observed to within ~5 nm of the surface.

Figure 1: PNNL 1.2" tall SCC tensile initiation specimen.

SCC Initiation Test Systems

Test systems have been built to allow in-situ monitoring of crack initiation in an environment that provides a high degree of control over load (stress), water temperature and water chemistry including B/Li content, dissolved gas content and impurity content. These test systems are very similar in design to systems built at PNNL to measure SCC of LWR pressure boundary component materials [1].

The key parts of these test systems are: (1) a servo-electric load control system capable of maintaining a stable constant load for very long periods of time and capable of providing a wide range of cyclic loading conditions, (2) a recirculatory water system that that is used to control water chemistry, (3) an autoclave for specimen exposure at high temperatures and pressures, (4) a direct current potential drop (DCPD) system for in-situ monitoring of crack initiation, and (5) a continuous data acquisition system. Careful consideration went into design and equipment selection to optimize control of all system variables. Some of the most important optimizations were to: (1) make sure that all wetted components release no contamination into the water, (2) have a sufficiently high water flow rate through the autoclave to maintain the target chemistry, (3) maintain uniform temperature and pressure at the specimens, (4) obtain highly accurate measurements of the test environment (temperature, conductivity, pH, load, dissolved gas content), and (5) create a sensitive DCPD crack initiation detection system. Each of the subsystems will be discussed in further detail below.

The water flow system is comprised of low- and high-pressure loops as shown in Figure 2, of which a side stream is taken off this low-pressure loop and fed into the high-pressure loop.. The purpose of the low-pressure loop is to flow water through a water column where selected gases and ionic impurities are dissolved or injected into the water. The large pressure pulses and flow

surges created by the piston pump are dampened by the use of pulsation dampers both at the inlet and outlet of the pump. The high-pressure water flows into a regenerative heat exchanger where hot water leaving the autoclave is used to preheat the incoming water. Just prior to entering the autoclave, the partially heated water is brought up to test temperature using a preheater. After the water flows through the heated autoclave, it goes back through the regenerative heat exchanger and then through a water cooler that brings the water back down to room temperature. The cooled water then passes through a back-pressure regulator and emerges at ~0.07 MPa (10 psi) of pressure. The water flows through a flow meter, a conductivity sensor, a mixed resin bed demineralizer, and is finally dumped back into the low-pressure mixing loop.

Boron (B) and lithium (Li) levels for PWR primary water testing are controlled by pre-saturating the mixed resin bed demineralizer with boric acid and lithium hydroxide to specific levels that will result in tailored near-constant B and Li content in the water. There is some drift in the Li level in the water because it is singly ionized and is easily displaced from the demineralizer by more highly positively ionized species coming off the autoclave such as chromate. The displaced Li is removed by periodic partial replacement of water in the mixing loop with water having little or no Li (and some B). Boron and Li levels in the mixing loop are determined from measurements of water conductivity, pH and temperature. Water flow through the autoclave is maintained at ~125 cc/min (two autoclave exchanges per hour) to provide a consistent chemistry environment.

DCPD Measurement

PNNL uses a reversing DCPD system developed by Peter Andresen of GE. As with all DCPD measurement systems, a constant current is run though the sample, however by using a solid-state polarity-reversing switch built into the current path, potential drop is measured in both a forward and reverse current flow condition. By taking the average of the voltage in the forward and reverse current conditions, contact voltages are eliminated from the measurement. Finite element modeling was used to visualize the voltage distribution in the interior of the specimen and on the surface. Wire attachment positions were selected in regions where voltage was relatively uniform on the surface thus making it relatively easy to remove and reinsert specimens for testing as needed without significantly changing the DCPD response. Platinum wire is used for current and voltage feeds into the autoclave. For PWR water testing, segmented transformation toughened zirconia (TTZ) tubing is used to help prevent shorting of the Pt wires against other wires or any metal surfaces in the autoclave. Some crosstalk in the voltage wires occurs and is minimized by keeping the wires separated as far as reasonably possible from each other. In addition, the current wires are kept away from the voltage measurement wires. A specimen is electrically insulated from the load train using ceramic spacers. Spot welding is used to attach the platinum wires to a specimen.

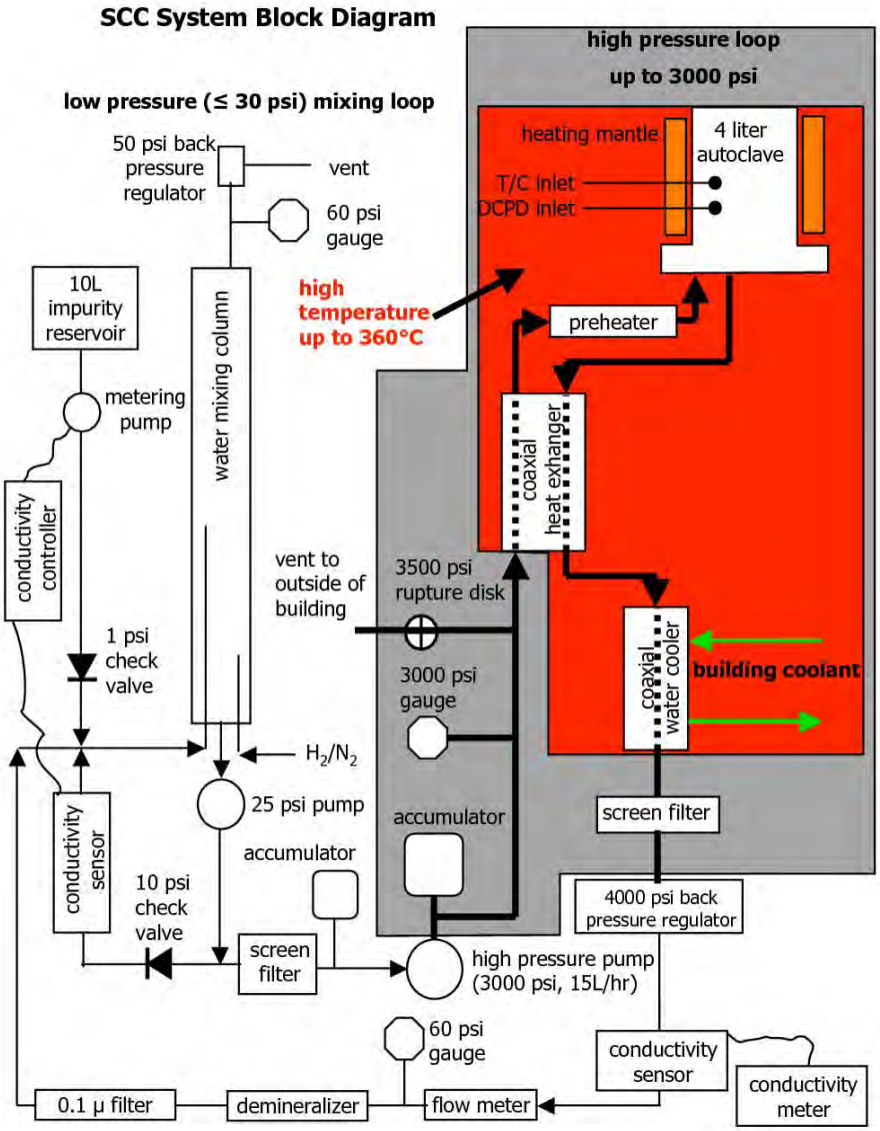

Figure 2: General water flow diagram for PNNL SCC crack-growth and initiation test systems.

A sketch of the final tensile geometry and how DCPD is applied is shown in Figure 3. The voltage across the gauge section, V_{gauge}, is sensitive not only to a change in the cross-sectional area of the gauge region due to crack formation, but also to changes in gauge length and diameter caused by tensile strain from plastic deformation. Although crack initiation is the phenomenon of interest, a crack initiation test is actually a creep test up until the point of crack initiation. The decision has been made that when reasonable, the DCPD data will be plotted in terms of strain with the understanding that crack initiation will produce a significant deviation from the creep strain trajectory. The relationship between gauge voltage and volume-conservative tensile strain is given by:

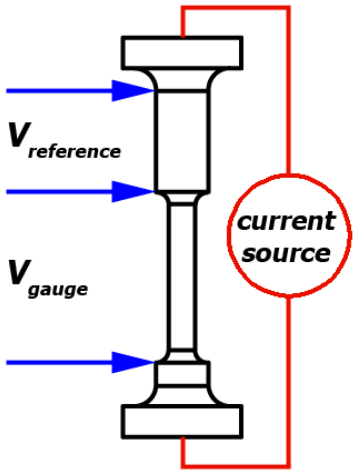

Figure 3: Schematic of tensile geometry and DCPD measurement points.

$$\varepsilon = \frac{1}{2}\ln\left(\frac{V_{DCPD}}{V_{DCPD_o}}\right) \tag{1}$$

There are some challenges to measuring the actual strain in the gauge section. DCPD voltage is not only sensitive to crack formation and creep strain, but it is also sensitive to changes in the resistivity of the material. Both alloys 600 and 690 are known to exhibit a change in resistivity when exposed to LWR-relevant temperatures, and while this must be due to changes in the alloy microstructure, these microstructural features have yet to be identified. In order to remove this resistivity-based DCPD change and ensure the highest possible degree of sensitivity in detecting crack initiation, the specimen was designed to have a region where the inherent resistivity of the specimen would be monitored and subtracted from the resistivity change of the gauge section. This is accomplished by having a region of the specimen with larger diameter where the stress is ~15% of the gauge stress. The formula for the reference-corrected strain is:

$$\varepsilon_{referenced} = \frac{1}{2}\left[\ln\left(\frac{V_{gauge}}{V_{gauge_o}}\right) - \ln\left(\frac{V_{ref}}{V_{ref_o}}\right)\right] \tag{2}$$

In this formula, V is a DCPD-measured voltage. Note that the reference DCPD voltage will be sensitive not only resistivity-driven changes, but it will also be sensitive to creep strains that occur in the reference region that is at ~15% of the gauge stress. Thus, a small amount of creep strain, if any is occurring at test temperatures (≤360°C), would be subtracted. It will also be sensitive to elastic strains that occur in the reference region. This formula has been found to work quite well at estimating the strain when the reference region has the same bulk microstructure as the gauge region.

Load Train

Load is applied using a servo-electric motor that can hold a steady load for indefinite periods of time while also providing the ability to perform cyclic loading in either position or load control up to about 3 Hz. Load from the servo-electric motor is transmitted into the autoclave with a pullrod that runs through the base of the autoclave, and the specimens are braced from above by a top plate and multi-bar linkage that transmits load from the top plate to the base of the autoclave. Two types of specimen loading systems were developed, one for testing 1-3 specimens, and another that was developed for testing up to 30 specimens using a single servo motor and autoclave. These systems are shown in Figure 4. Both system designs rely on series loading to allow multiple specimens to be tested with a single servo motor. All specimens in the 1-3 specimen load train can be simultaneously monitored with DCPD, while due to the cost and challenges associated with running a very large number of Pt wires, the 30 specimen system is currently limited to monitoring up to 16 specimens. Series loading of the 1-3 specimen load train is straightforward with all specimens supported in a single string. The 30-specimen load train utilizes three strings of 10 specimens. All three strings are firmly bolted to the upper support plate while the bottom of the strings is attached to a plate that is allowed to pivot around the load rod and the ends of each of the three strings using ball joints. This equilateral triangle arrangement forces all three strings to carry 1/3 of the load generated by the servo motor. Since not all specimens can be monitored simultaneously, each string is designed so that if a specimen cracks to the point of failure, the string will pick up the load and allow the test to continue. Because of the self-supporting feature, any number of specimens can be tested up to 30.

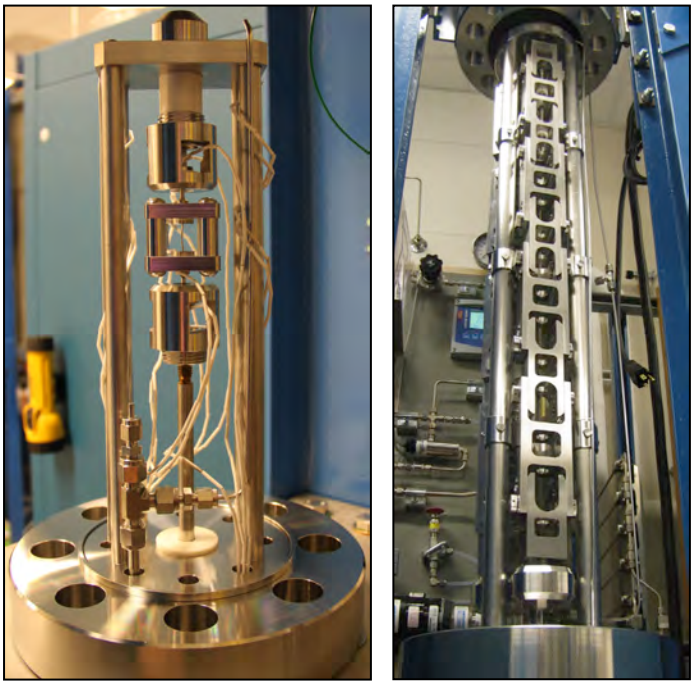

Figure 4: Load train for crack initiation test systems at PNNL for (a) 1-3 specimens and (b) up to 30 specimens.

Corrosion Test Systems

Two modular high-temperature environmental chambers capable of exposing at least twenty corrosion coupons in controlled high-temperature water environments are attached to existing high-temperature crack growth test systems. These systems were assembled and are operated in conjunction with our ongoing Basic Energy Sciences project at PNNL. Placement of the environmental chamber in the process flow water flow path enables the environmental chamber to be operated at temperatures independent of the crack growth test system. A series of high temperature valves permit isolation of this environmental chamber from the crack growth system at any time during a crack growth test sequence. As a result, corrosion tests can be performed for various time periods independent of the crack growth test system.

Overview of Characterization Approaches

All samples were prepared for SEM/TEM/APT analysis using FIB milling. The samples were sputtered with a thin layer (~50 nm) of Pt and then cross-sectional samples ~10-15 μm wide x 5 μm in depth were removed from the surface and thinned to electron transparency. The TEM grids were placed in a specially fabricated holder that mechanically clamps the grid and orients it normal to the SEM pole piece. This allows low-kV SEM-BSE imaging without damaging the grid or using tapes or epoxies. Using low-kV BSE imaging provides high resolution imaging (~5 nm), while probing the top ~10-200 nm depending upon accelerating voltage. Rapid morphological investigation of the penetrative oxidation layer is achieved and the shallow interaction volume assists in discriminating projection issues in subsequent TEM and APT investigations. Scanning TEM (STEM) in conjunction with energy dispersive spectroscopy (EDS) was performed on site-specific grain boundary FIB lift-outs. APT analysis was also performed on site-specific grain boundary and surface locations in order to help elucidate the chemistry and microstructure of oxides along with compositional changes in the metal ahead of the oxidation front. Distinct similarities in surface oxidation structures were observed for all of the Ni-30Cr alloys examined. SEM, TEM and APT examples will be presented highlighting important aspects of the observations with most results shown for the GE alloy 690MA + 20%CR material. However, comparable structures could have been given for the other alloys unless differences are identified in the text.

Characterization of Corrosion Nanostructures for Alloy 690 Materials

Corrosion tests have been conducted on a wide range of alloy 690 and alloy 600 materials in simulated PWR primary water conditions (1000 ppm B, 2 ppm LiOH). Various temperatures (325-360°C) and exposure times (100-5000 hours) have been evaluated. The dissolved hydrogen concentration has been selected to correspond to the Ni/NiO stability line at each temperature. For this report, only results for certain alloy 690 materials will be described focusing on test results after a 1000-hour exposure in 360°C PWR primary water with a dissolved hydrogen concentration of 25 cc/kg H_2.

SEM Examination of Surface Oxidation

Each of the exposed surfaces illustrated some degree of transgranular (TG) penetrative oxidation. Figure 5 shows representative cross-section SEM-BSE images of the penetrative oxidation on both the GE alloy 690MA + 20%CR and the as-received CRDM alloy 690TT materials. The morphology of the oxidation appeared as a dual layer microstructure. The outer layer consisted of faceted spinels that were typically less than half a micrometer in size although sporadic crystals on the order of several micrometers were observed. The inner portion was much more complicated, with a thin layer (~10 nm thick) just below the outer layer followed by penetrative filamentary oxidation into the bulk grains. The exact thickness and location of this thin layer can be difficult to quantify in SEM due to the similar contrast of the inner and outer oxide layers, and a dashed yellow line has been added to indicate the interface between these layers. It is noted that the start of the bulk grain contrast is a key indicator of this film thickness (as shown by the bottom arrow in Figures 5a and b). The 1000-h exposures produced TG penetrative oxidation reaching ~50-100 nm in depth and was similar for all alloys examined. Penetration depths approaching 1 μm been observed at after longer exposure times, especially in crack wall microstructures [4]. In comparing materials with and without cold work, there are some differences in the morphology of the penetrative oxidation. The corroded cold-worked specimens exhibited a more dense, filamentary oxide network into the bulk grain as illustrated in Figure 5(a). This is in contrast to oxide filaments that tend to be very linear and well spaced in the as-received, non-CR materials (Figure 5b).

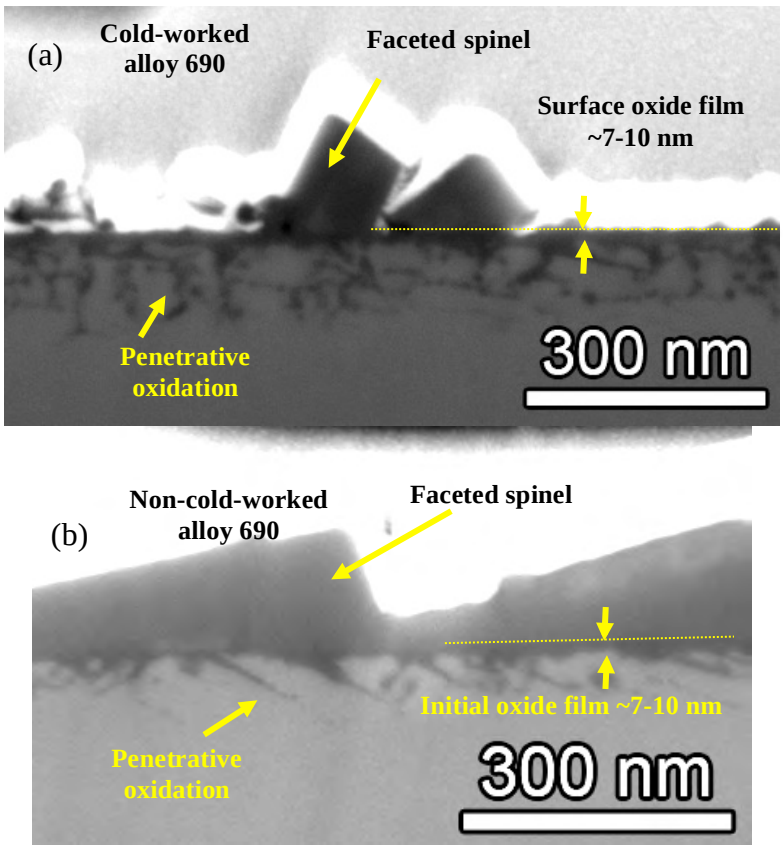

Figure 5: SEM micrographs illustrating the cross-section surfaces for (a) GE alloy 690MA + 20%CR and (b) as-received CRDM alloy 690TT materials exposed for 1000 h to 360°C simulated PWR primary water. A thin continuous oxide film is present in contact with the metal along with large faceted particles on the outer surface.

Oxide morphologies were also extensively examined at locations where grain boundaries intersected the surface (Figure 6). Localized corrosion or intergranular attack (IGA) was not observed in any material, nor was TG penetrative oxidation detected within ~100 nm of the grain boundary intersection. The TG penetrative oxidation was fairly uniform across the exposed grain, but then decreased as the grain boundary was approached. Although IGA did not occur, the high-energy grain boundaries intersecting the surface were influenced by the exposure to high-temperature PWR primary water. SEM-BSE images revealed a contrast change along one side of the grain boundary to depths ranging to 0.5-1 μm from the surface. The contrast difference suggested local depletion of Cr and Fe and consequent Ni enrichment. This feature along with the bowed boundary appearance is believed to be indicative of grain boundary migration and has been observed in a wide range of exposure examples. Detailed TEM and APT characterizations of the migrated boundaries have been performed and will be discussed later in this section. In summary, all random, high-angle grain boundaries intersecting the surface did show evidence for composition changes below the oxide and a lack of penetrative oxidation in the vicinity of the boundary. The most significant variability among observations resulted from the density of IG Cr carbides at the boundary particularly for the CRDM alloy 690TT material.

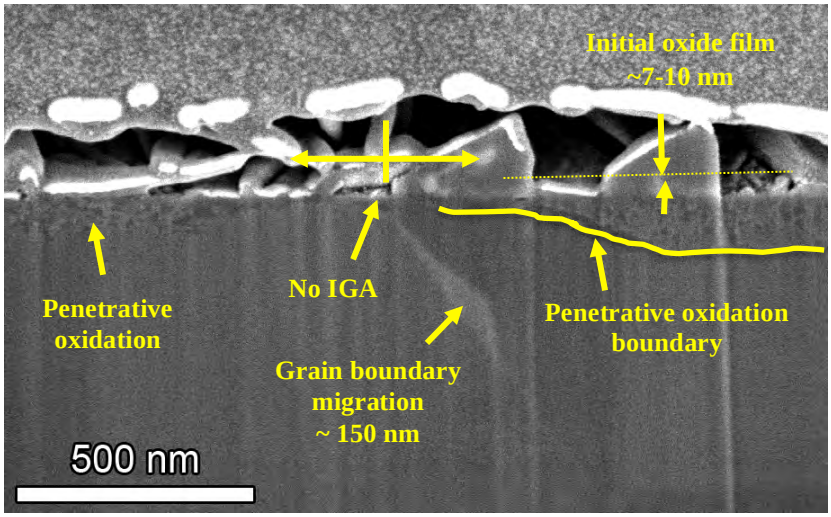

Figure 6: SEM micrograph illustrating the cross-section surface and near-surface grain boundary of the GE alloy 690MA + 20%CR material exposed to 360°C simulated PWR primary water for 1000 h.

Lastly, representative 20 kV SEM-BSE images of exposed surfaces are shown for three different materials in Figure 7. From the surface, the trace outline of the grain boundaries intersecting the surface can be observed in all three materials. The bright contrast accenting the grain boundaries in each case is Ni enrichment (due to Cr and Fe depletion). The bright contrast on either side of the grain boundary in the Ni-30Cr and CRDM samples is the 20kV beam probing through the surface oxide and into the base metal below (as opposed to the beam probing both penetrative oxidation and metal in the bulk grains). There is much narrower bright contrast width at the grain boundaries in the GE alloy 690MA + 20%CR sample and cross-section exams show the penetrative oxidation extends closer to the grain boundary. The high density of dark “particles” along the grain boundaries in the CRDM material is believed to be IG Cr carbides and the very low density of such particles in the GE alloy 690MA material is consistent with its microstructure (few IG carbides).

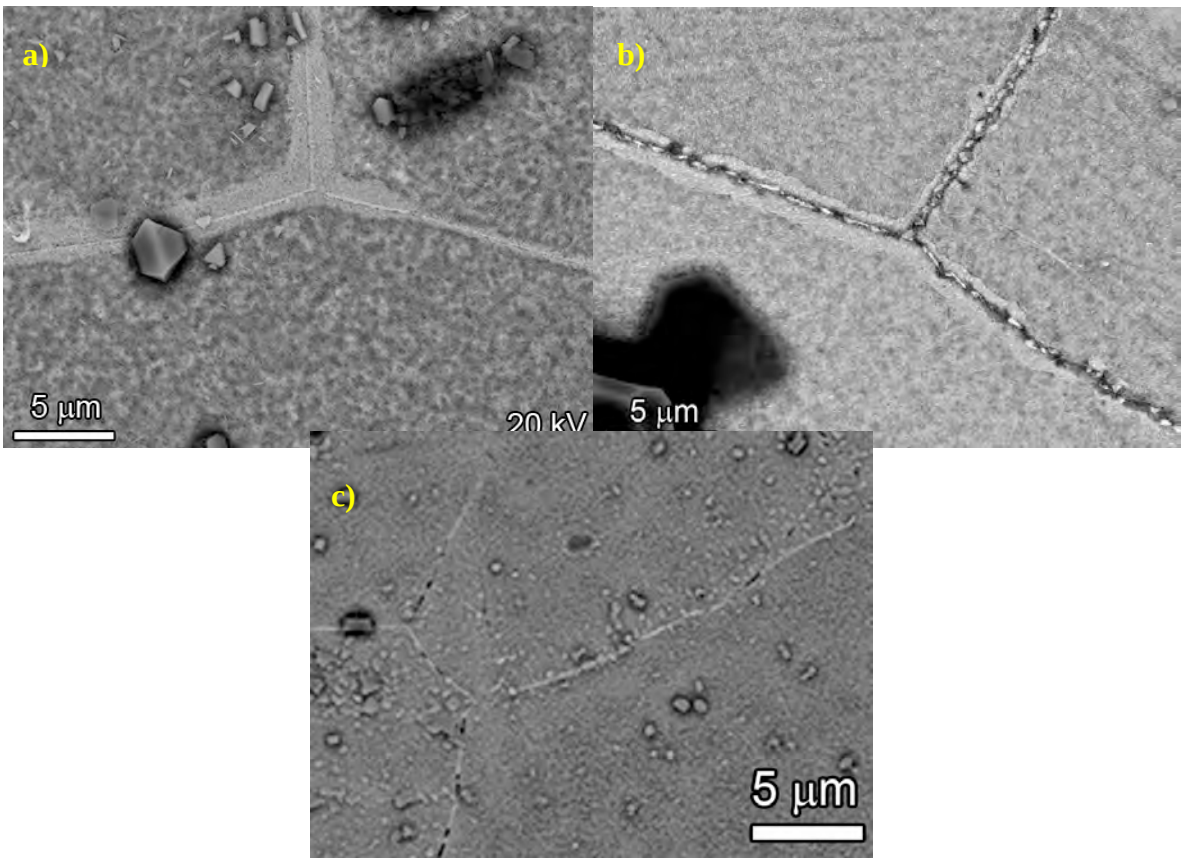

Figure 7: SEM-BSE micrographs showing the corroded surfaces for the (a) Ni-30Cr, (b) as-received CRDM alloy 690TT and (c) GE alloy 690MA + 20%CR materials.

TEM Examinations of Surface Oxidation

As has been demonstrated in the SEM-BSE images of exposed cross-sectional surfaces, the oxide microstructure appears different at the exposed grains than at the exposed grain boundaries. It is apparent that a thin, continuous film (~10 nm) was present over the entirety of the surface, however BSE contrast is not sensitive enough to distinguish the oxide microstructure. TEM of cross-sectional FIB samples prepared containing high-energy grain boundaries was utilized to demonstrate that a thin film of chromia (Cr_2O_3) is formed at the surface/boundary intersection and that Cr depletion is present just below the exposed surface. Similar structures were discovered in all materials although the presence of IG carbides at the surface made TEM characterizations more difficult in the CRDM alloy 690TT specimens. The best example of the continuous thin film formation and grain boundary migration was observed in the Ni-30Cr sample. Figures 8-10 present the same boundary using TEM and SEM-EDS imaging. The contrast showing the bowed, migrated boundary is apparent in Figure 8 and corresponds with the extent of Cr depletion observed in Figures 9 and 10. The thin (7-10 nm) film of oxide formed across the surface of the sample was identified as oriented Cr_2O_3 and

darkfield imaging of this phase showed a uniform oxide film on the surface of the lower grain in Figure 8. It is unknown as to why the darkfield imaging does not extend across the entire grain, but it could be due to local strains rotating the grain slightly out of a diffracting condition. The STEM/EDS maps (Figure 9) and linescan across the depleted boundary (Figure 10) clearly illustrate the extent of the Cr depletion, with the initial grain boundary position indicated by the straight line on the top of the image and the final bowed grain boundary position near the bottom. For this particular grain boundary migrated region, measured Cr drops to ~5 wt% across the 55 nm depletion zone from ~29 wt% in the adjacent matrix.

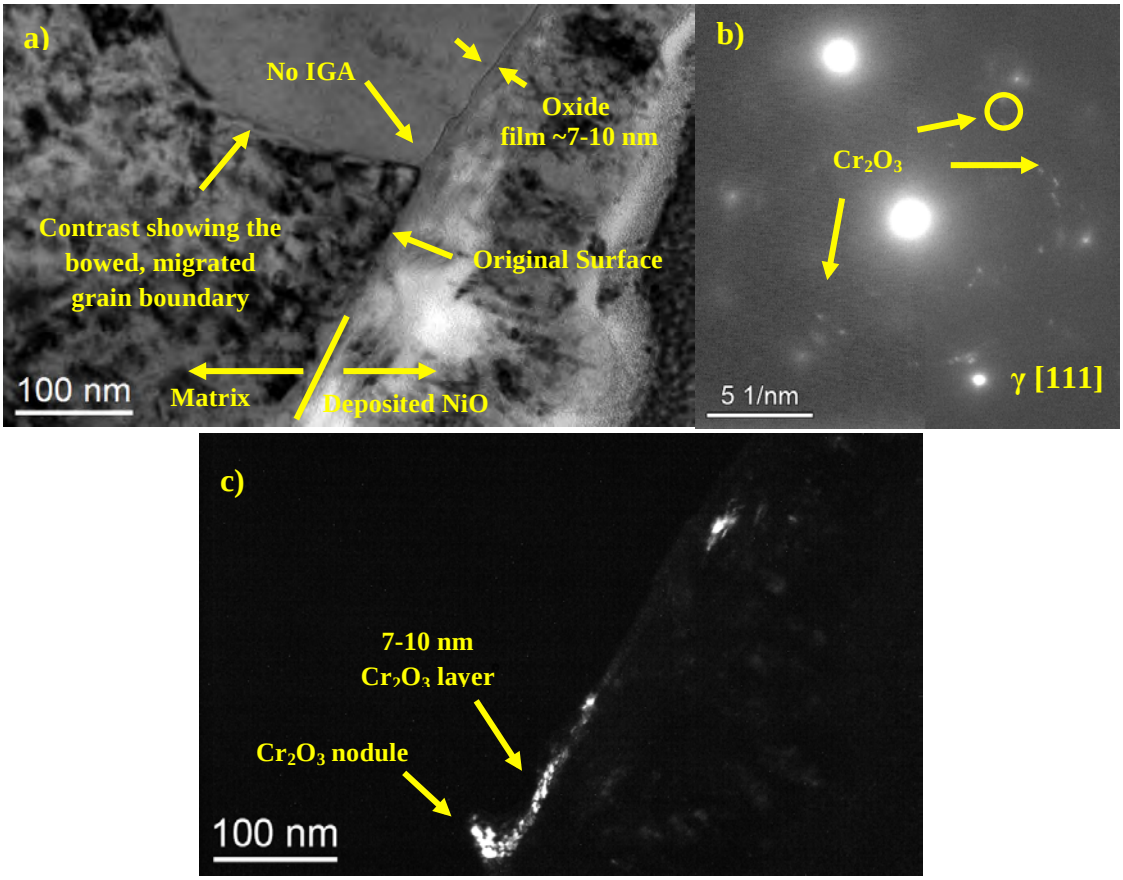

Figure 8: Brightfield/darkfield pair of Ni-30Cr grain boundary exposed for 1000 h in 360°C PWR primary water. a) Brightfield image showing bowed grain boundary contrast, 7-10 nm oxide film and no IGA. b) Selected area diffraction taken from bottom most grain and thin film in a) showing the matrix grain tilted to the [111] orientation and Cr_2O_3 oriented oxide. c) Darkfield image showing continuous chromia film across part of the surface of the oxide.

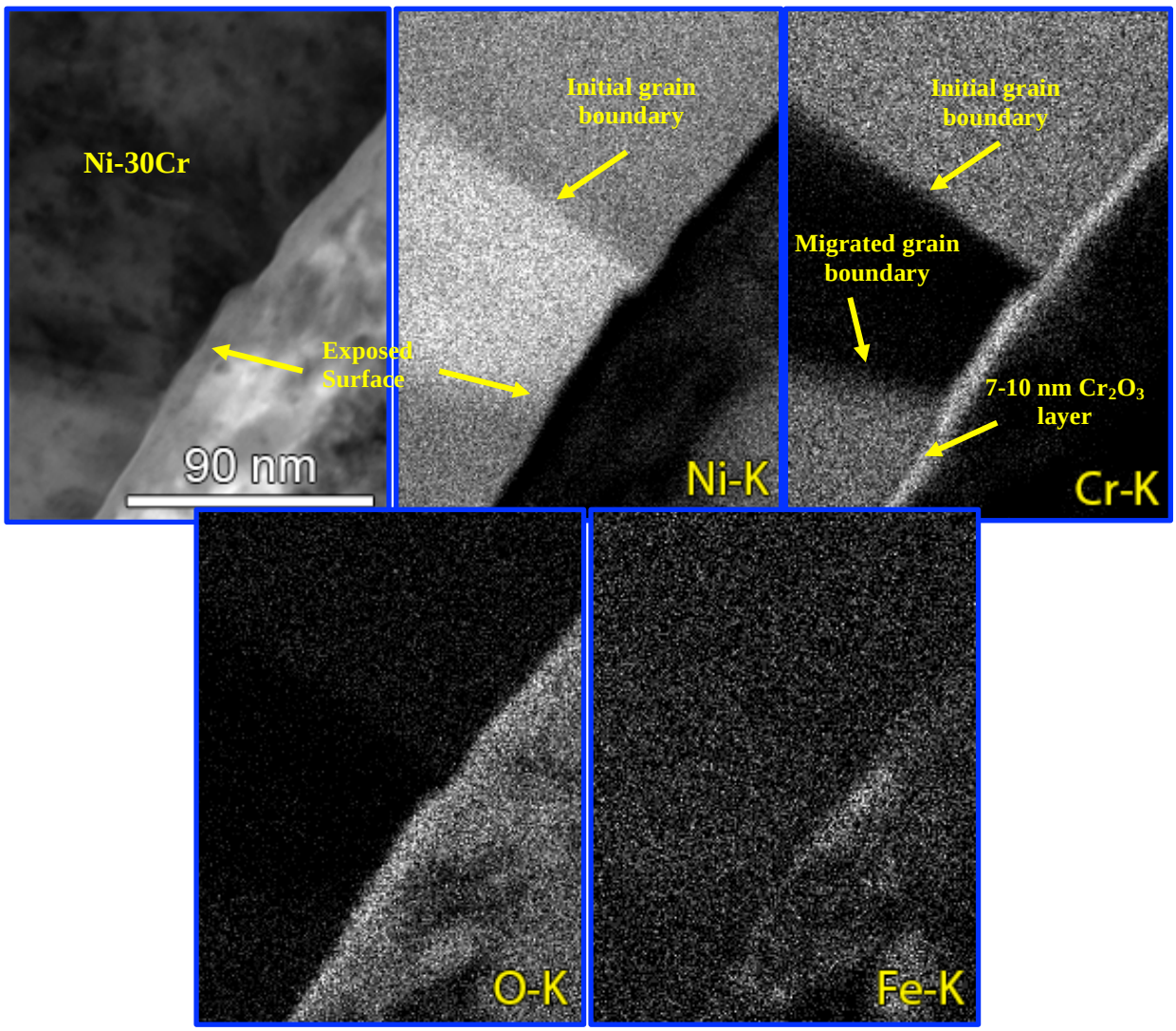

Figure 9: STEM image and EDS elemental maps illustrating compositional variations across the cross-section surface of Ni-30Cr exposed to 360°C PWR primary water for 1000 h. The extent of the grain boundary migration is evident from the Cr depletion. The continuous Cr_2O_3 thin film is observed across the sample surface.

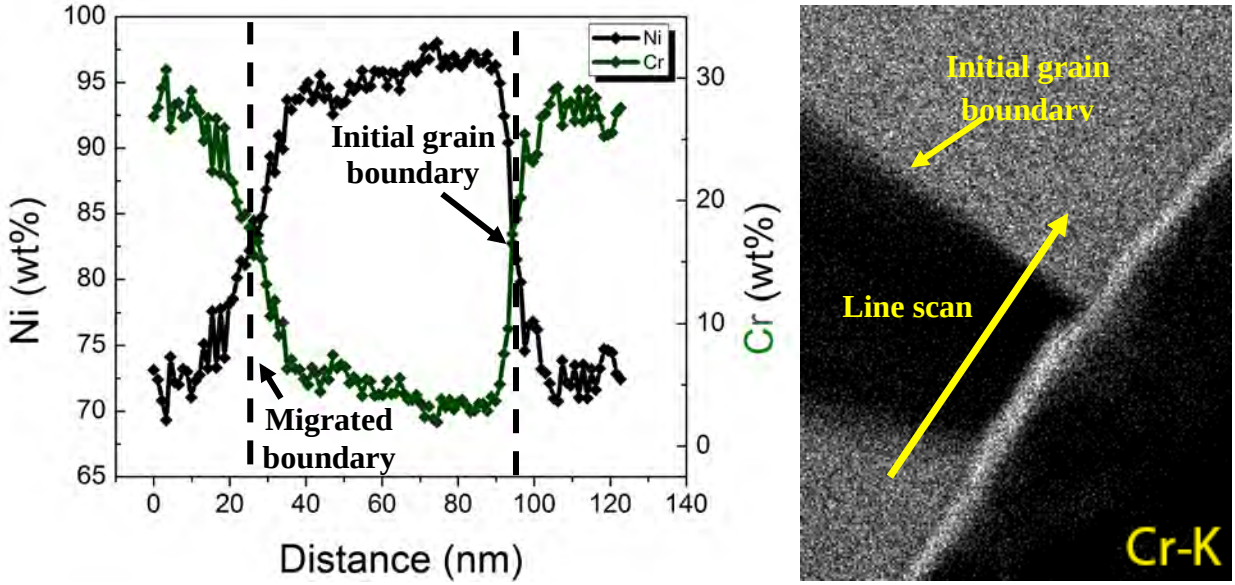

Figure 10: STEM/EDS linescan across the migrated grain boundary in Figure 8(a) near the exposed surface showing the extent of the Cr depletion. The grain boundary was highly inclined and could not be tilted on edge, hence the wide Cr profile across the interface.

Similar Cr depletion was observed in alloy 690 samples as shown in Figure 11, which is a STEM/EDS elemental map of a grain boundary/surface intersection in the ANL alloy 690MA + 26%CR specimen. A narrow region (10 nm wide) of grain boundary Cr (and Fe) depletion can be seen extending ~300 nm below the surface oxide with Cr levels dropping to ~10 wt%. In this instance, the Cr-rich oxide layer on the surface appears to be more of a cap of oxide instead of a thin film. The best indication of its extent can be seen in the Figure 11 Ni-K map. The dashed arrows highlight the beginning of the oxidation (i.e., where the Ni metal signal begins laterally in relation to the grain boundary), suggesting that the Cr-rich oxide cap is ~150 nm wide and ~50 nm in thickness. The original metal surface is marked with a dashed line in the Ni, Cr and Cr/Fe difference maps. The surface oxide layer above the TG penetrative oxidations is ~10 nm thick (which matches well with the SEM observations) and is best observed in the Cr/Ni difference map. Diffraction analysis in this region determined that the thin oxide film is no longer continuous Cr_2O_3, but consists of islands of Cr_2O_3 and fine grained MO structure or spinel oxide similar to what has been observed in crack wall oxides [4,5]. Lastly, the surface spinels were measured to be Ni/Fe rich (contrast in Ni-K map was adjusted to show TG penetrations), hence spinel contrast was minimized. The composition of the oxide films and near-surface grain boundaries will be discussed in the APT section.

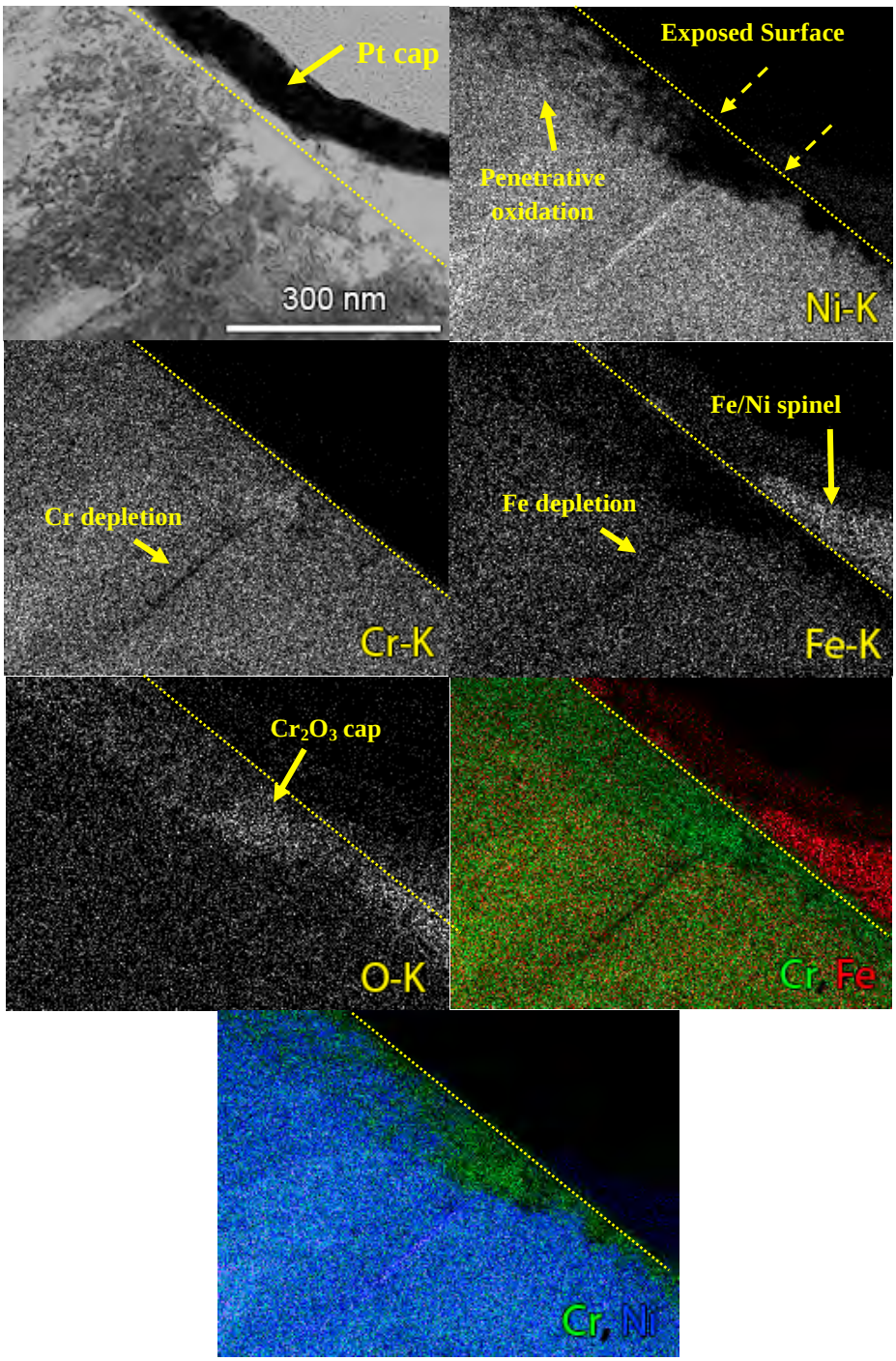

Figure 11: STEM image and EDS elemental maps illustrating compositional variations across the cross-section surface of ANL alloy 690MA + 26%CR exposed to 360°C PWR primary water for 1000 h.

Additional TEM characterizations have been conducted on the GE alloy 690MA + 20%CR specimen to illustrate surface and near-surface oxidation microstructures. A brightfield TEM image of a corroded TG surface cross-section in Figure 12(a) illustrates a large faceted spinel on the surface. The thin film oxide just below the spinel is not readily apparent in this image due to the strong diffraction contrast of the penetrative oxidation layer just below the surface, which extends ~100 nm from the surface. A slightly mottled contrast is also exhibited for the metal matrix due to high dislocation densities as a result of 20% cold work in the bulk material. The extent of the penetrative oxidation is more easily observed in an underfocused (-1024 nm) brightfield TEM image in Figure 12(d). The sample was tilted to a kinematic condition in order to minimize contrast within the metal, thus allowing the difference in density of the oxide filaments to be imaged in the underfocused condition. Darkfield imaging using the Cr_2O_3 and MO (rock salt) reflections are illustrated in Figures 12(b) and 12(c), respectively. The Cr_2O_3 platelets are crystallographically aligned to the alloy matrix and only one of the variants is imaged in Figure 12(b). Despite imaging only one of eight variants, a high density of 5-10 nm thick, discontinuous platelets of chromia is readily apparent throughout the penetrative oxidation. When the MO reflection is used for DF imaging (Figure 12c), it is observed that the oxide appears nanocrystalline and continuous, forming filaments. Lastly at the sample surface, the continuous oxide film is comprised primarily of MO phase oxides with islands of Cr_2O_3.

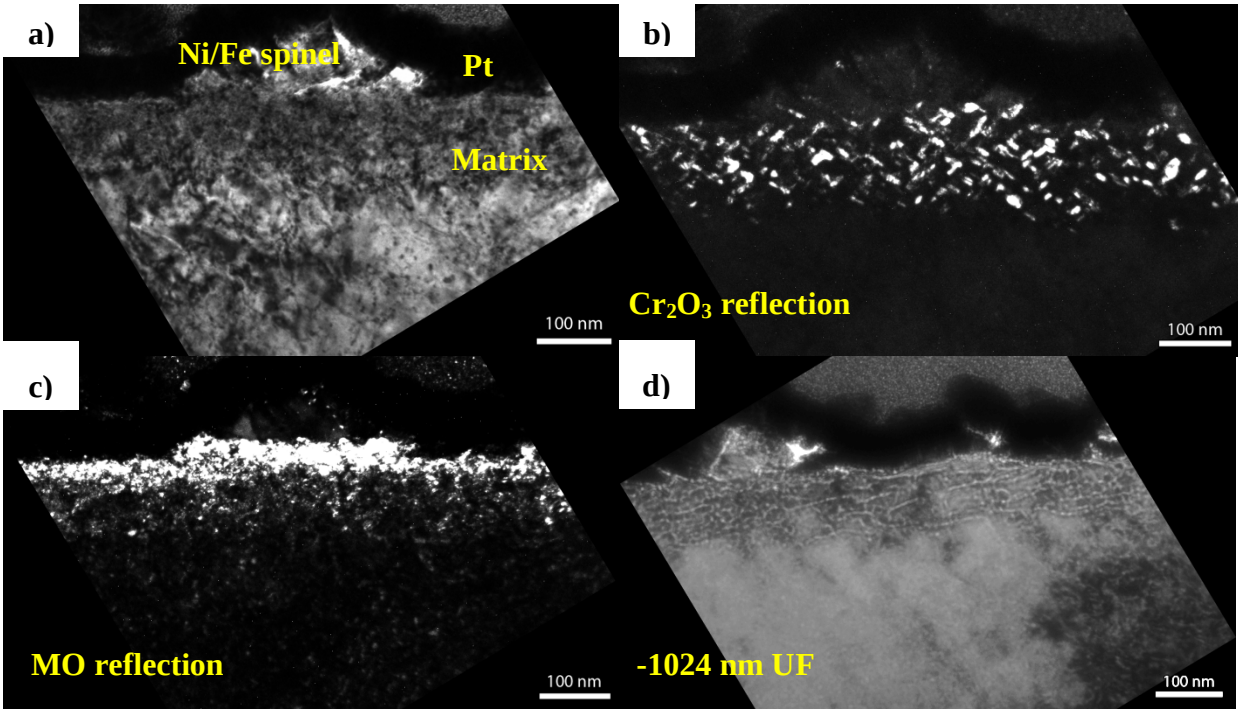

Figure 12: TEM micrographs (Fresnel contrast imaging and DF images) highlighting the dual phase oxide structure of the penetrative oxidation. a) brightfield, b) MO-structure oxide darkfield, c) Cr_2O_3 darkfield (only one variant). d) Underfocused BF image showing the extent of the filamentary penetrative oxidation from the surface.

STEM EDS elemental maps depicted in Figure 13 illustrate the compositional changes in the metallic grain boundary associated with corrosion in PWR primary water. The STEM brightfield image reveals that the grain boundary is not straight and kinks ~150 nm from the sample surface. The STEM EDS elemental maps demonstrate that the bright contrast apparent along the grain boundary by SEM corresponds to Cr depletion and Ni enrichment that extends along the grain boundary beyond the ~400 nm field of view for this image. Comparing the width of the Cr depletion with the grain boundary position from the STEM brightfield image suggests that the grain boundary has migrated. It also can be seen in the maps that the large surface spinel oxides are Fe rich.

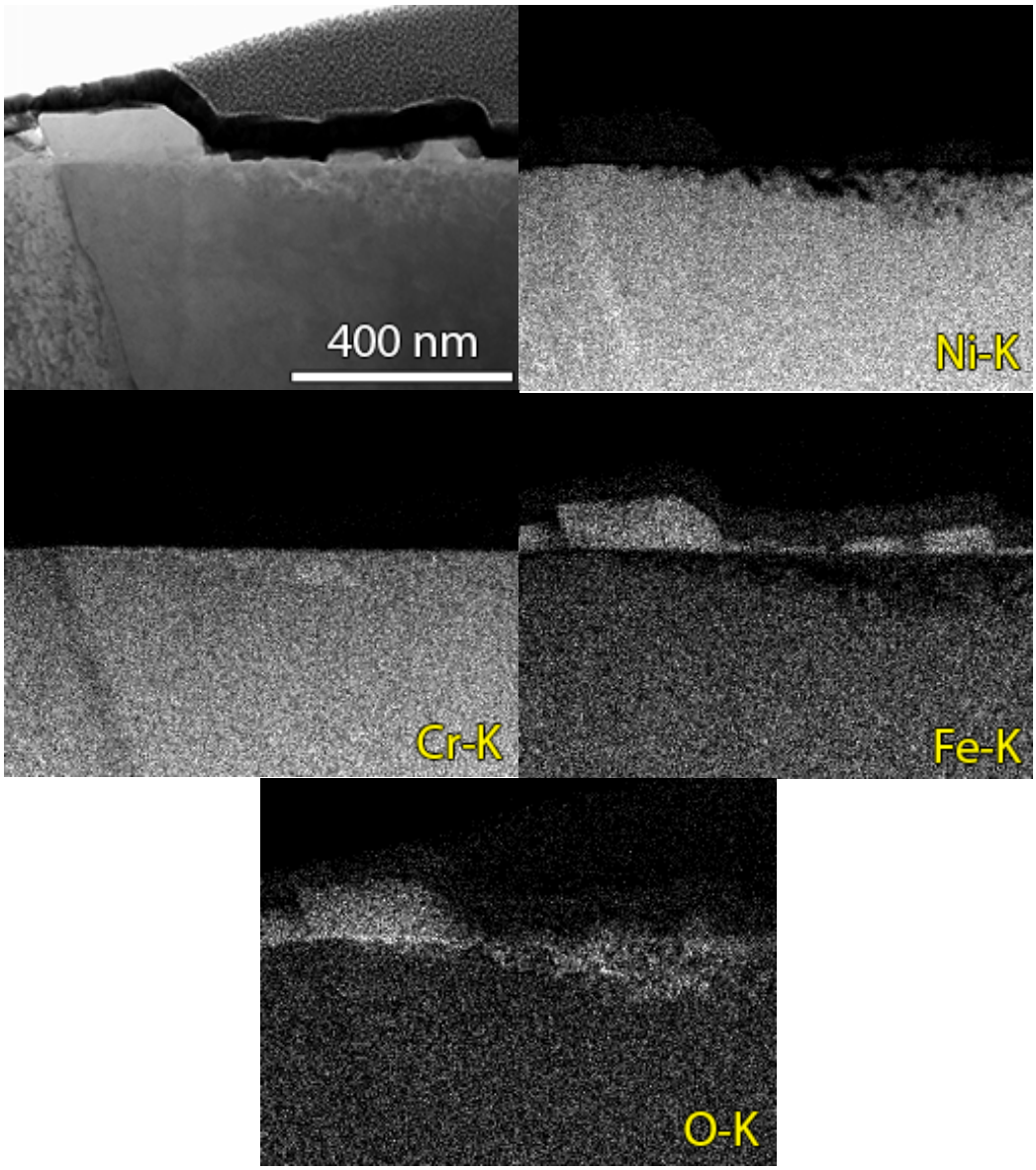

Figure 13: STEM image and EDS elemental maps illustrating the penetrative oxidation and an intersection of a grain boundary with the exposed surface of the cross-section surface. The extent of the grain boundary migration is evident from the Cr depletion. No IGA is observed.

Consistent with the SEM-BSE examinations on this specimen, penetrative oxidation is not observed by STEM-EDS at or near the grain boundary intersection with the surface. The onset of penetrative oxidation into the matrix is best visualized with the EDS O-K elemental map and by the STEM brightfield image. Along the surface at ~400 nm from the grain boundary, O-rich filaments are clearly apparent extending ~100 nm into the matrix. STEM-EDS mapping also shows localized Fe and Ni depletion in these regions indicating that the oxide is Cr rich. Most importantly, there is no O enrichment or IGA along the grain boundary below the surface film.

Diffraction and darkfield imaging (Figure 14) was performed to ascertain the crystal structure of the Cr-rich oxide observed in Figure 13. The brightfield TEM image shown in Figure 14(a) is of the same region as the STEM BF image in Figure 13, with a large surface spinel crystal serving as a fiducial marker just to the right of the grain boundary. Figure 14(b) shows the darkfield image of a Cr_2O_3 reflection that illuminates the continuous thin oxide film just below the surface spinel. This region correlates well to the strong Cr-K and O-K maps in Figure 13. At ~100-150 nm from the grain boundary, the continuous Cr_2O_3 becomes discontinuous and the surface oxide film contains islands of Cr_2O_3 (similar to the oxide microstructure in the filaments).

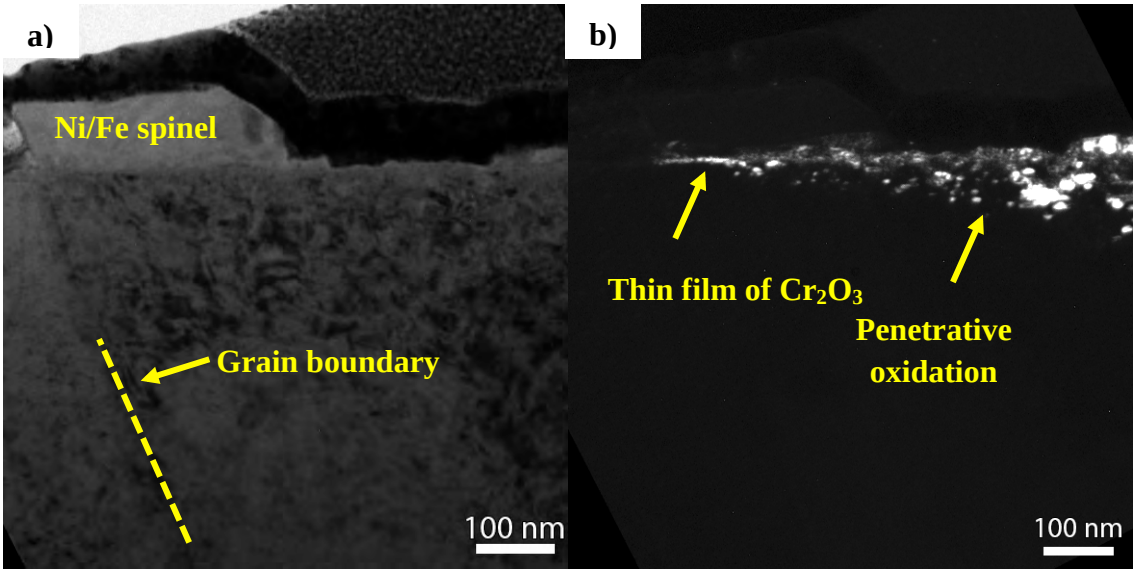

Figure 14: Brightfield/darkfield pair of the exposed surface. a) Brightfield image showing bowed grain boundary contrast, 7-10 nm oxide film and no IGA. b) Darkfield image showing continuous chromia film across part of the surface of the oxide.

Lastly, a continuous oxide layer was observed on the perimeter of the penetrative oxidation. The SEM-BSE and darkfield images in Figure 15 examine a similar region adjacent to a grain boundary at high magnification. The continuous oxide layer appears to have formed after significant penetrative oxidation and is comprised of relatively large grains of Cr_2O_3. From the darkfield image, it is apparent that the chromia film formed at the surface is comprised of larger platelets that do not all satisfy the same diffracting condition (i.e., imaging of a single diffraction spot does not illuminate all of the individual oxide crystals). The individual Cr_2O_3 crystals are larger in the continuous oxide layer at the perimeter than in the penetrative oxide filaments themselves. Since the continuous film is only observed along the penetrative oxidation closest to the grain boundaries, it is likely that Cr has diffused from the grain boundary along the metal/oxide interface to supply the additional Cr needed.

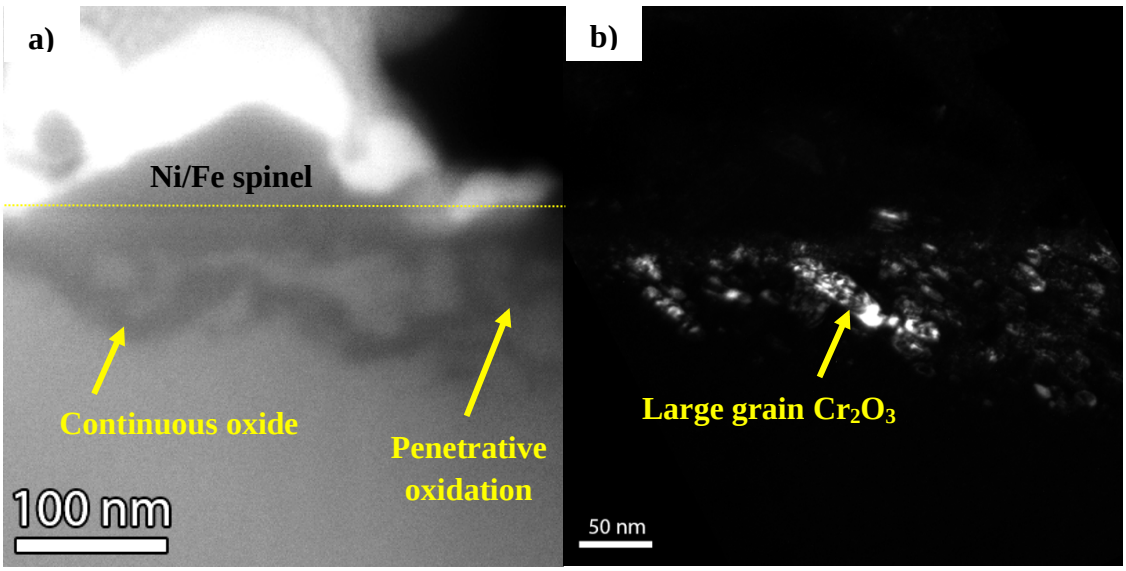

Figure 15: Electron micrographs illustrating the continuous oxide adjacent to the penetrative oxidation a) SEM BSE image showing continuous oxide that appears at the perimeter of the penetrative oxidation near grain boundaries. b) Darkfield image of the continuous oxide that is comprised of larger grains of Cr_2O_3 as compared to the platelets observed in the penetrative oxidation. The grain boundary is located ~100 nm from the left edge of these images.

APT Examinations of Surface Oxidation

APT analysis was performed for most materials at the intersection of a grain boundary with the exposed surface to investigate the subsurface compositional changes below the oxidation front. An APT reconstruction where a grain boundary intersected the surface in the GE alloy 690MA + 20%CR sample is depicted in Figure 16. Detected ions of CrO (blue) are used to illustrate oxidized regions of the sample, while the metal matrix is illustrated with Ni ions (green). The white dashed line indicates the grain boundary location. Isoconcentration surfaces at Cr+O = 85 at% (red ribbons) delineate a continuous layer of Cr_2O_3 (~5 nm thick) that covers the grain boundary. At the grain boundary, oxygen ingress terminates within 10 nm of this surface.

Several grain boundaries of alloy 690 have been analyzed within 10-200 nm of its intersection with the exposed surface. A representative dataset for the GE alloy 690MA material is described in Figure 17. This example demonstrates extensive depletion of Cr, Mn and Ti accompanying the formation of the protective film of Cr_2O_3 and other surface oxides. However, no evidence is found for O into the metallic grain boundary or O-Cr cluster precursors. The extensive grain boundary depletion is accompanied by diffusion-induced migration of the boundary. This is made apparent by the distinctive bowing of the interface in Figure 17. Complementary TEM analyses have confirmed crystallographically that the straight interface was the previous grain boundary location prior to the dealloying process, and the bowed interface is its new position after extensive depletion. Overall, Cr has been depleted from ~31 at% in the matrix to less than 7 at% (<50 nm from surface) and 18 at% (~200 nm from surface) (Figure 18). Minor Fe depletion is also observed along with the nearly complete depletion of minor elements Mn and Ti in this grain boundary example.

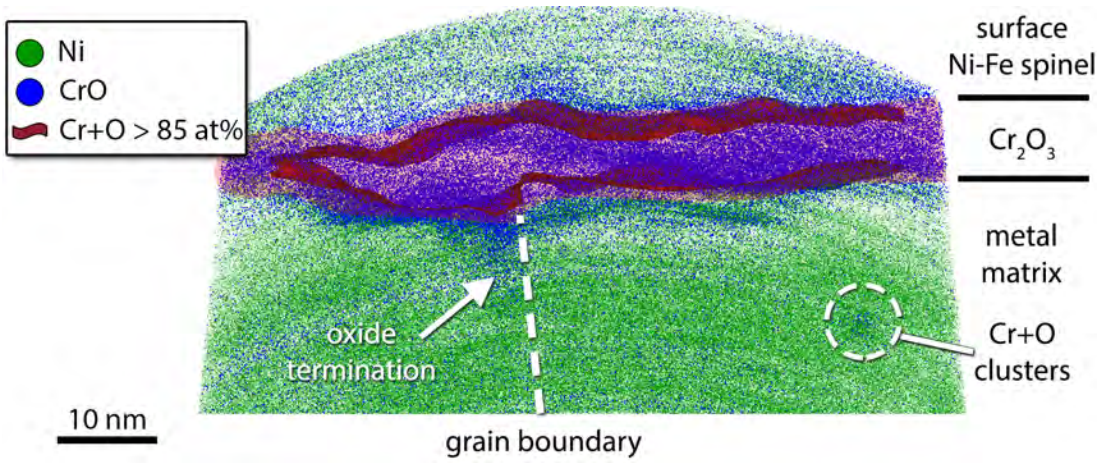

Figure 16. Atom map of intersection point of a grain boundary with the exposed surface in the exposed 20%CR GE alloy 690MA material. A protective layer of Cr_2O_3 has formed over the grain boundary, protecting it from oxygen penetration.

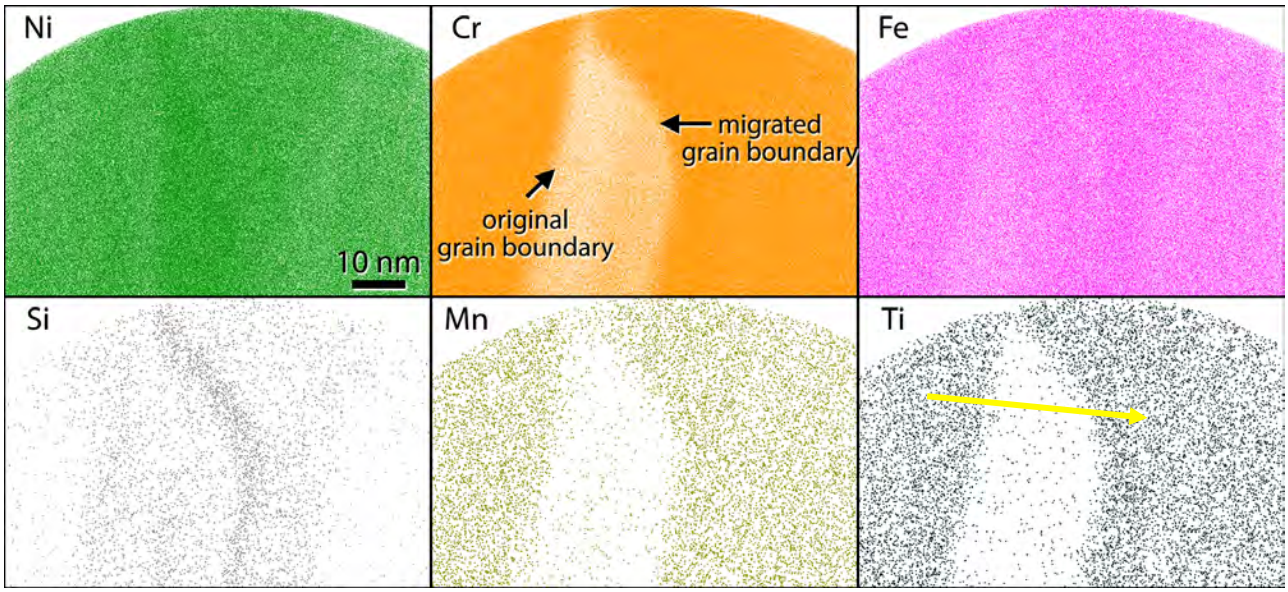

Figure 17. Atom maps (10 nm image depth) of the same grain boundary in Figure 16 at a distance of ~50 nm from the surface. Significant depletion of Cr, Mn and Ti has accompanied the apparent grain boundary migration.

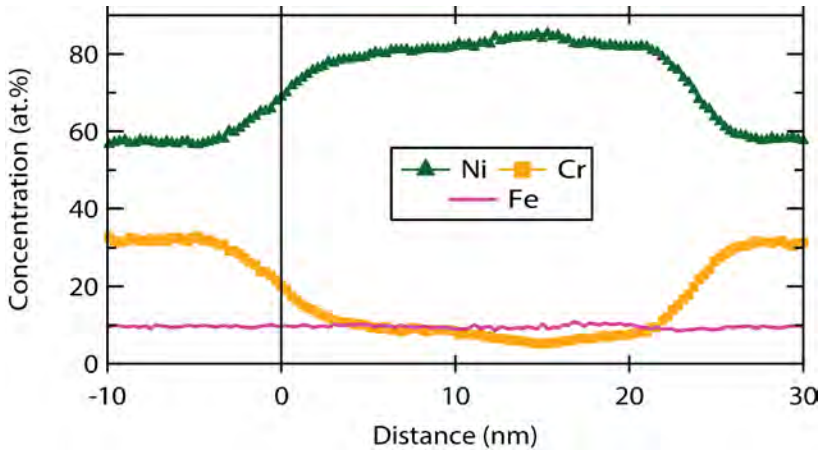

Figure 18. 1D concentration profile across the grain boundary and dealloyed zone depicted by the dashed arrow in Figure 17. The Cr concentration is depleted to ~10 at% in this zone from ~31 at% in the matrix, while Ni is strongly enriched compensating for the depleted alloying elements.

The surface oxidation of alloy 690 in close proximity to grain boundaries (within ~200 nm) typically exhibited no TG oxide penetrations in SEM and TEM exams. A representative APT reconstruction of this surface location is presented in Figure 19 and isolated shallow oxide penetrations were discovered as shown in individual atom maps (a), a composite atom map (b) and isoconcentration surfaces (c). Five unique regions with oxidation structures can be identified. The outer surface oxide is composed primarily of Ni-Fe spinel (most likely $NiFe_2O_4$). A 25-nm diameter cuboidal NiO particle is also apparent at the sample surface, surrounded by the Ni-Fe spinel. In general, NiO particles were present in very low density in comparison to the more ubiquitous Ni-Fe spinel on the exposed surface. A third oxide region is a nearly continuous layer of Cr_2O_3 along this section of the specimen surface. Small, shallow penetrations of Cr-rich oxide are seen beneath this layer and are directly connected to the surface Cr_2O_3 layer.

A concentration profile (Figure 20) was also produced from the metal/oxide interface to illustrate the oxide composition along with local segregation/depletion in the metal. From left to right, the profile measures the local composition of the surface Ni-Fe spinel, the Cr_2O_3 layer, and the mixed region of metal with shallow O penetration. The Ni-Fe spinel is observed to contain a moderate concentration of Cr (~8 at%), which may be a result of its close proximity to a grain boundary. The Cr_2O_3 layer exhibits a higher O concentration (~56 at%) compared to the Ni-Fe spinel (~52 at%) indicative of the chromia phase. Subtle segregation was present at the metal/Cr_2O_3 and Cr_2O_3/spinel interfaces. At the metal/oxide interface, strong segregation can be seen for Mn (oxide side) and Cu (metal side) of the interface.

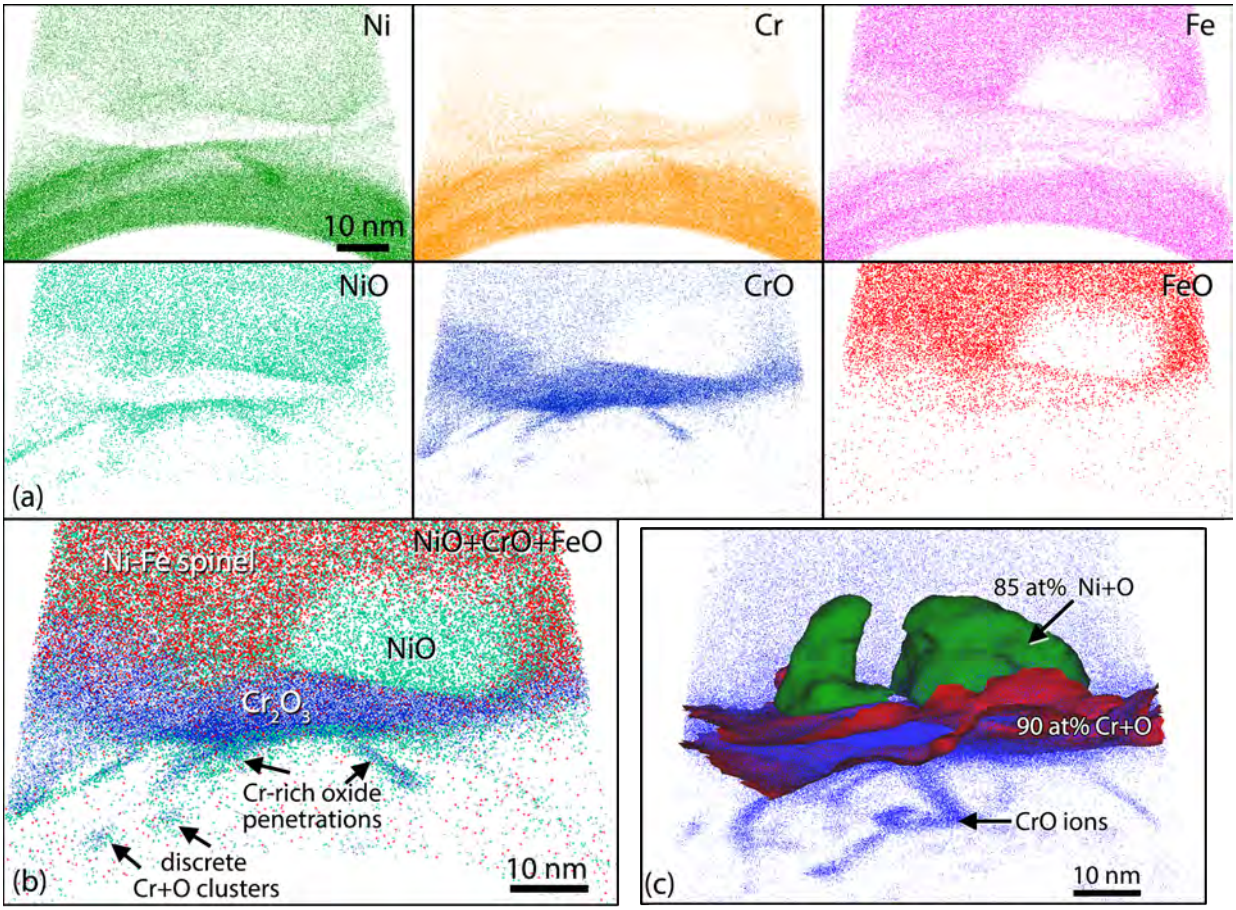

Figure 19. (a) Individual atom maps from an APT reconstruction of surface oxidation in the GE alloy 690MA + 20%CR material in close proximity to a grain boundary (~200 nm). (b) Composite atom maps of NiO, CrO and FeO signals from (a) indicating that three distinct oxide phases are present: a surface Ni-Fe spinel, a surface NiO, and a continuous film of Cr_2O_3. (c) Isoconcentration surfaces at 85 at% Ni+O (green), 90 at% Cr+O (red) with CrO atom map (blue).

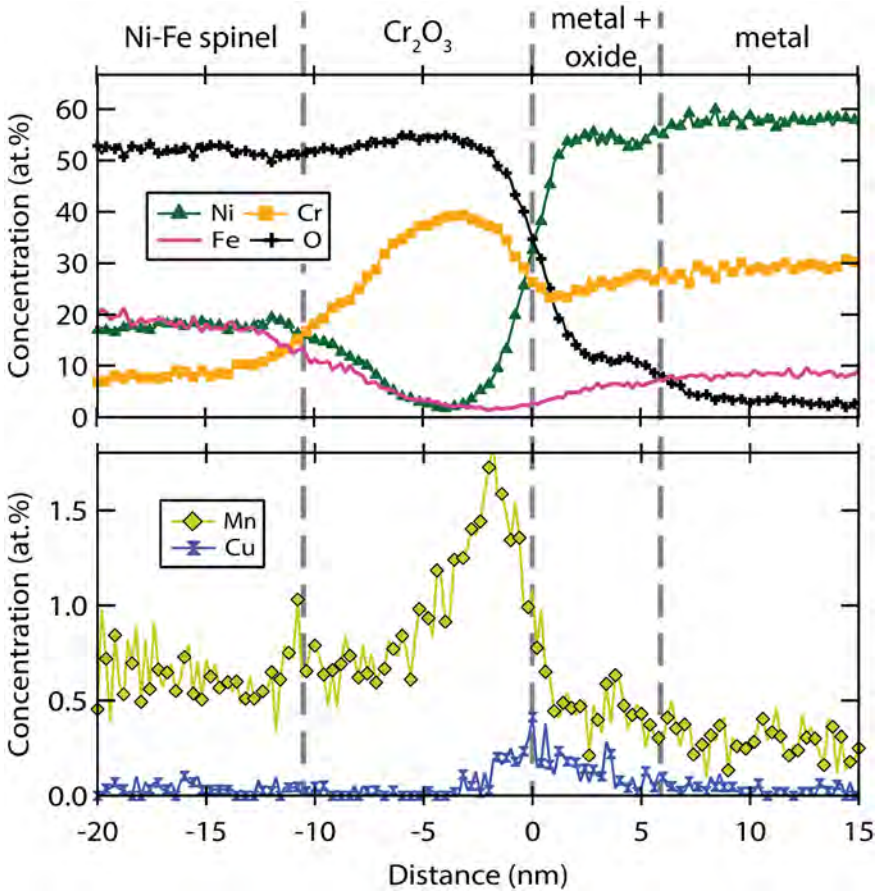

Figure 20. Representative 1D concentration profile across the metal/oxide interface at a grain boundary/surface intersection in the GE alloy 690MA + 20%CR material. Three distinct regions are apparent: a Ni-Fe spinel external oxide, a layer of Cr_2O_3 and minor oxygen into the matrix along small penetrations. Interfacial segregation is apparent at the metal+oxide/Cr_2O_3 interface (Cu and Mn).

Further from the grain boundary, alloy 690 exhibits deeper oxide penetrations and only isolated regions of Cr-rich oxide consistent with Cr_2O_3 at the surface. A representative APT reconstruction take several micrometers away from the nearest grain boundary is exhibited in Figure 21. Deep, penetrative oxide penetrations are present extending from a Ni-Fe spinel into the metal in the ~100 nm field of the view for this reconstruction. Isoconcentration surfaces drawn at 90 at% Cr+O (red) delineate several discrete Cr_2O_3 precipitates within the interconnected, filamentary oxide penetrations. TEM diffraction analysis of similar regions has identified the interconnecting oxide regions as nanocrystalline, oriented MO-phase oxides, while the Cr_2O_3 platelets were observed to be crystallographically oriented to the metal matrix. Importantly, no continuous surface layer of Cr_2O_3 was observed in any APT dataset taken far from the intersection of a grain boundary with the surface.

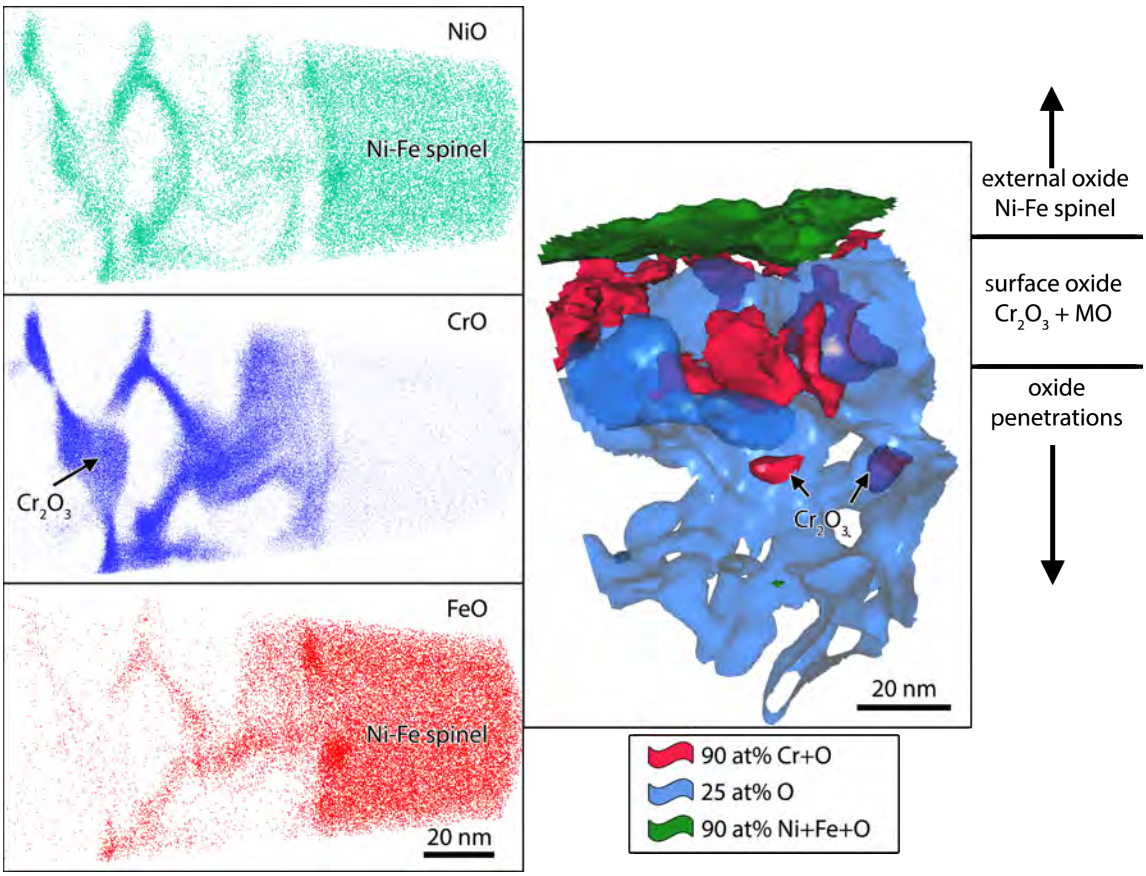

Figure 21. Atom maps (left) and isoconcentration surfaces (right) from APT analysis of surface oxides in GE alloy 690MA material at a representative matrix location far from a grain boundary. Instead of forming a continuous film of Cr_2O_3, discrete islands of Cr_2O_3 formed near the sample surface accompanied by extensive oxide penetrations into the metal matrix below.

Discussion of Alloy 690 Corrosion Test Results

Alloy 690 has been found to be highly resistant to SCC initiation and propagation in PWR primary water environments both from service experience and laboratory testing. This enhanced corrosion resistance is typically accepted as being the result of a protective Cr-rich oxide that forms over the surface. Surface science experiments (e.g., x-ray photoelectron spectroscopy, secondary ion mass spectroscopy, etc.) have illustrated the existence of this behavior in both PWR primary water conditions and supercritical water, however these analyses focus on overall bulk surface oxidation [6-8]. In order to better understand the microstructure of these films, electron microscopy analysis has been performed to achieve the vertical spatial relationships of the oxides formed to the exposed bulk surface [8-14]. From these experiments, the corrosion has been described as having a bi-layer structure, consisting of external and internal oxide layers. The external layer, typically depending on autoclave material, is comprised of faceted Ni/Fe rich spinels that have a cube/cube orientation relationship with the internal layer. The internal layer has been described as a mixed iron and nickel chromite ($Ni_{(1-x)}Fe_xCr_2O_4$) which has a cube/cube

orientation to the matrix below. Selected research has identified small islands of chromia (on the order of 5-10 nm) in between the internal layer and the matrix. Lastly, there have been conflicting reports of a Cr depletion layer below the internal oxide layer [10,12-14]. With that being said, there are very few electron microscopic investigations of grain boundary corrosion microstructures during exposure to PWR primary water chemistry. In regards to SCC initiation, it is believed that understanding the corrosion characteristics of grain boundaries is of utmost importance.

Through the combination of high-resolution SEM-BSE imaging, TEM/EDS analysis and APT of exposed coupons of alloy 690 materials, corrosion-induced oxidation structures are clearly shown to be different at grain boundary/surface intersections than over bulk matrix grains. In previous research, the internal layer at crack walls and polished surfaces was much more complex than a single layer of oxide [11]. While the matrix surface layer most likely begins as a uniform Cr-rich mixed oxide, penetrative oxidation proceeds into the bulk grains demonstrating that a protective stable oxide does not form at these highly polished surfaces. Current research revealed that a continuous, protective chromia film does form at the surface over high-energy grain boundaries. The overall surface oxide film characteristics for alloy 690 materials exposed to PWR primary water are illustrated in the Figure 22 schematic with a continuous Cr_2O_3 film above grain boundaries and a mixed oxide film above the matrix regions with isolated pockets of Cr_2O_3 along with filamentary oxidation into the metal.

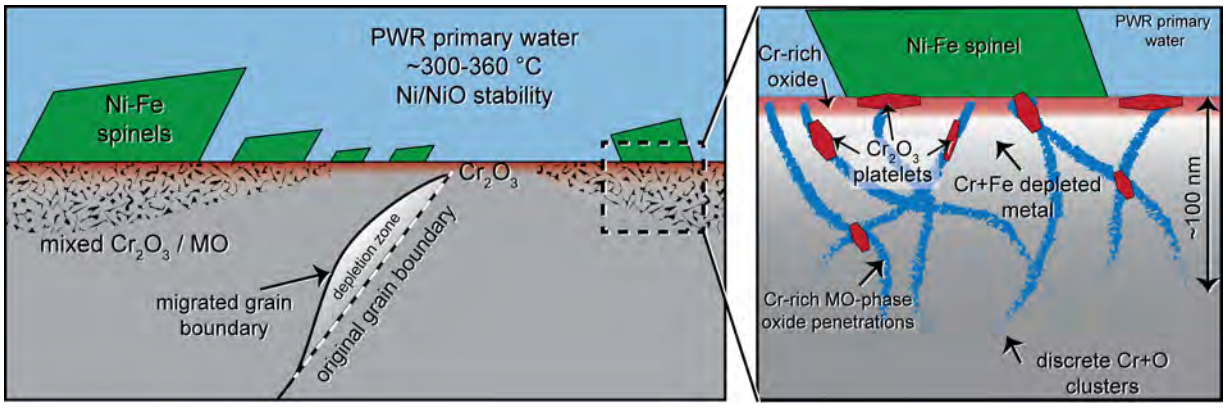

Figure 22. Enhanced Cr diffusion from grain boundaries allows protective Cr_2O_3 film (~0.5-1 μm wide) to form over grain boundary. Non-protective thin film of Cr_2O_3 and Cr rich MO forms over bulk grains due to slower Cr bulk diffusion. Oxygen diffusion through non-protective film allows penetrative oxidation to occur in bulk grains. Additionally, increased Cr diffusion continues along grain boundary to edge of protective film and forms continuous Cr_2O_3 layer between bulk and penetrative oxidation.

From these distinct microstructural features, several insights have been determined as to how grain boundaries behave when exposed to high-temperature PWR primary water conditions. There is a zone above high-energy grain boundaries where a continuous protective chromia film forms blocking IG and TG penetrative oxidation. This has been consistently observed on cross-sections of as-received and cold-worked alloy 690 materials with highly polished surfaces. It is believed that during initial exposure, Cr diffuses rapidly along the grain boundaries to the surface and forms a protective Cr_2O_3 layer that spans ~200 nm on either side of the grain boundary. Past this near-boundary region, the amount of Cr diffusing from the bulk matrix grains is not sufficient to immediately form a protective layer and a mixed oxide surface layer forms that enables local TG penetrative oxidation into the metal matrix.

In these 1000-h exposures, characterizations indicate that there are isolated islands of Cr_2O_3 and possibly of metal islands within the inner oxide above the bulk grains. If the closest metal islands were to be used as a fiducial mark in the corroded materials, the inner Cr-rich surface oxide would be somewhere between 10 to 50 nm in thickness with thicker films for the highly cold-worked materials and thinner for the as-received materials. TEM data indicates that the matrix mixed oxide inner layer is primarily a MO-structure oxide, but APT analysis has shown that chemically it relates closer to the M_3O_4 spinel. Regardless, the fact that it is not comprised of continuous Cr_2O_3 allows for O ingress and penetrative oxidation possibly along preexisting dislocation structures. This formation of Cr_2O_3 islands has been suggested previously to exist in between the internal spinel layer and the alloy 690 matrix. Exposures of surfaces at high O_2 potentials have shown similar chromia islands surrounded by a MO microstructure [15]. A critical difference between current and prior surface oxidation studies has been the initial surface condition. It is clear that deformed/disturbed surfaces promote more rapid Cr diffusion to the surface and alter formation of the Cr-rich inner layer film. It is believed that this rapid Cr diffusion in the altered surfaces could be an explanation for reported Cr depletion layer below the inner oxide layer [14]. Experiments are underway evaluating corrosion structures in alloy 690 materials as a function of surface grinding conditions that produce a highly deformed metallic subsurface with near-surface nanocrystalline grains.

This research illustrates unique observations of the formation of surface oxide (both above grain boundaries and bulk grains) on highly polished coupons when exposed to simulated PWR water conditions at high temperatures. Understanding the resultant thin film oxide microstructures as well as Cr depletion along grain boundaries intersecting the surface provides a good basis for identifying crack initiation precursors in SCC testing. In order for IGSCC initiation to occur, the protective chromia film formed over the grain boundaries must be cracked or thinned such that water can access the Cr depleted grain boundary below. The subsurface grain boundary, which is typically depleted to 5-10 wt% Cr, should be much more susceptible to corrosion and crack nucleation. An iterative process can be envisioned where IG crack advance can proceed through the depleted grain boundary until sufficient Cr is available to reform the protective Cr_2O_3 film at the tip. The formation and growth of the chromia film would again produce a Cr depleted grain

boundary ahead of the oxidation front and create a situation where the process can be repeated. A critical issue for this precursor microstructure to promote IGSCC is the applied stress and dynamic strain required to breach the protective film. Based on service experience and laboratory test results for alloy 690, it appears that local grain boundary Cr depletion near the surface is not a sufficient condition to promote a high susceptibility to SCC initiation in PWR primary water.

Experiments are underway to investigate static and dynamic loading effects on IGSCC initiation processes in alloy 690. Preliminary SCC initiation testing is described and discussed in the following section focused on cold-worked alloy 690 material conditions shown to be susceptible to SCC growth.

SCC Initiation Tests on Alloy 690 Materials

General Approach for SCC Initiation Testing for Alloy 690

Development of the DCPD tensile initiation test system and test method began with alloy 600 tests. As outlined in a previous report [16], crack initiation of cold worked alloy 600 was successfully detected in less than 2500 hours for several constant load tests where the specimens were held just below the yield stress. Because cold worked alloy 690 can exhibit crack growth rates comparable to cold worked alloy 600, the initial approach for alloy 690 crack initiation testing was similar to that of the alloy 600 for the cold-worked material condition, specimen surface preparation and general test approach.

Experimentation was started on two highly CR alloy 690 materials that exhibited high SCC propagation rates (~$1x10^{-7}$ mm/s) during crack growth rate testing in simulated PWR primary water at 360°C [1,2]. Materials selected were the 26%CR ANL plate and the 31%CR CRDM RE243 tubing. Composition and basic microstructural information on these two heats (NX3297HK12 and RE243) was summarized in Tables 1 and 2. These two materials are unique in that SCC behavior has been evaluated at multiple laboratories and their cold-worked microstructures have been extensive characterized [1]. Examples of the damage induced by cold rolling are illustrated in Figures 23 and 24 for the Valinox CRDM and ANL plate, respectively. The ANL material exhibited extensive permanent damage due to cold rolling including void formation at grain boundary carbide interfaces, cracked grain boundary carbides and cracked TG nitrides. Even though these voids and cracked precipitates were not directly responsible for the high IGSCC growth rates [2], this damage could make IG crack initiation more likely.

The intent for the first tests was to start with known highly SCC susceptible materials, and run them at the highest possible stress (near the yield stress) to produce a baseline minimum crack initiation time for alloy 690. Testing on these two specimens, IN006 (ANL plate) and IN007 (Valinox CRDM), began in April 2012. Approximately two months later, additional tests (IN009-IN012) were started on these same alloy 690 materials along with the GEG B25K heat

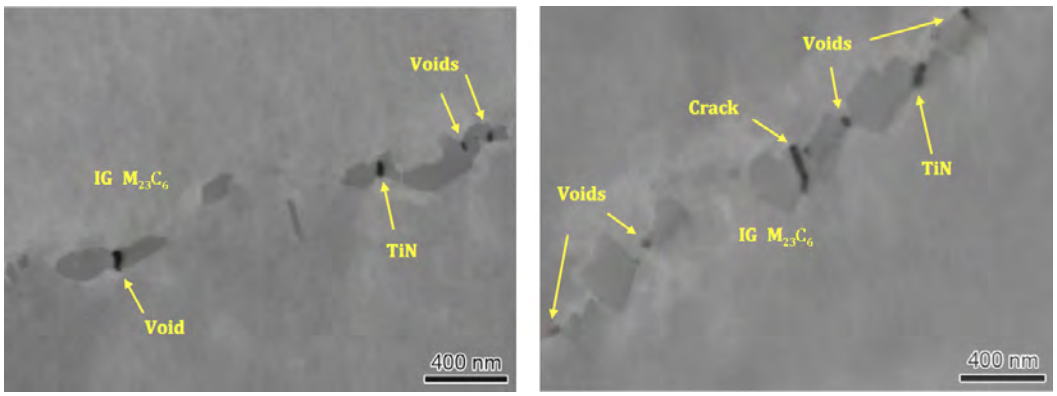

Figure 23. SEM-BSE images of the Valinox 31%CR alloy 690TT CRDM material showing voids and cracked carbides on grain boundaries in this material.

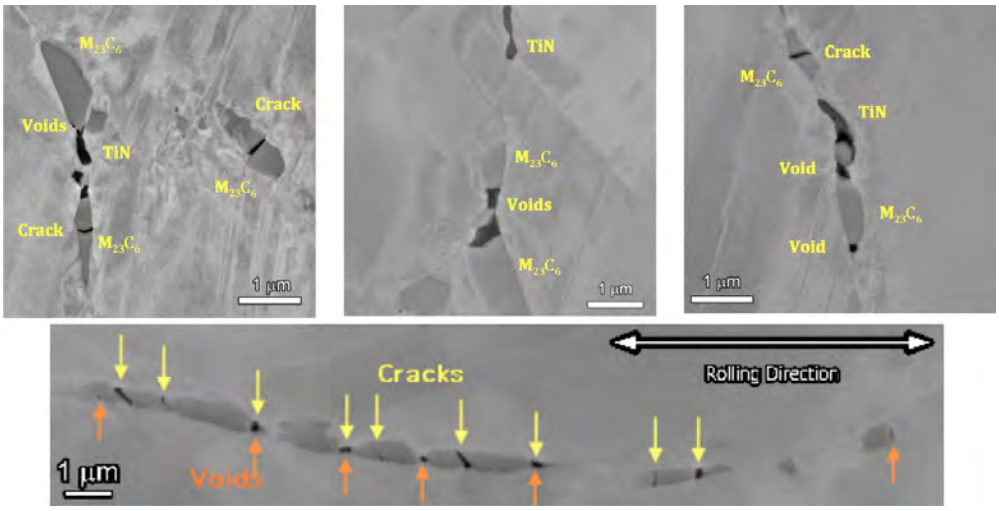

Figure 24. SEM-BSE images of the ANL 26%CR alloy 690MA plate material showing voids and cracked carbides on grain boundaries in this material.

(also described in Tables 1 and 2) in cold tensile strained condition. Corrosion and surface oxidation was investigated for each of these materials after exposure to 360°C PWR primary water as described in the previous chapter.

When 3600 hours of exposure for the known susceptible CR alloy 690 specimens (IN006/IN007) at or near the yield stress had not produced crack initiation, alternate testing conditions were considered. Because unstressed samples had revealed that a protective Cr_2O_3 film formed at grain boundaries intersecting the surface, it was decided to evaluate dynamic straining as a means to accelerate the crack initiation testing process. For the CR alloy 690 specimens, it was decided to begin periodically inducing very small amounts of plastic tensile extension. More aggressive methods (load cycling within the elastic strain region and slow, continuous plastic straining) were explored on the tensile strained alloy 690 specimens and will be discussed below.

Another aspect of the crack initiation testing approach on alloy 690 has been periodic inspections of the specimens to look for initiation precursor microstructures, in particular, to look for small cracks that might not yet have been detected by DCPD. Examinations were initially limited to documenting the surface of the gauge section using SEM, however after small cracks had nucleated from corroded TiN particles, it was decided to employ FIB milling to create shallow trenches to probe the structure of these cracks in cross section. The trenches were quite small, typically ~5-10 μm wide in both directions on the surface and ~5 μm deep, and present minimal if any stress riser on the specimen or the crack. This technique enables surface and near-surface SCC precursor damage to be investigated without destructive sectioning that would render continued testing impossible.

SCC Initiation Test Results on SCC Susceptible Alloy 690 (IN006, IN007)

As part of ongoing research for other programs, the SCC crack growth resistance of alloy 690 is being assessed [1]. Through this testing it has been found that the SCC susceptibility of alloy 690 greatly increases when it is cold rolled or cold forged and then crack growth tested in the pancake plane (S-L orientation for cold-rolled material). As noted above, two CR heats that exhibited crack growth rates of ~$1x10^{-7}$ mm/s were selected for the first alloy 690 crack initiation tests. Specimen IN006 was cut from the 26%CR ANL alloy 690MA plate and IN007 was cut from 31%CR CRDM alloy 690TT tubing. Specimens were machined into the 1.2" tensile geometry so that the normal to the rolling plane was parallel to the axis of the tensile specimens, and then the gauge sections were finished with 1 μm diamond polish. The polishing process leaves minimal surface damage and SEM-BSE imaging was able to reveal the grain boundary carbide structure as shown in Figure 25. TiN particles were also observed and often had a stringer shape perpendicular to the specimen axis in the alloy 690 plate specimen, while they were typically block shaped in the alloy 690 CRDM. As will be shown later, the TiN stringers in the plate material were found to act as microcrack initiation sites during in-situ plastic straining.

The specimens were loaded in series as illustrated in Figure 4. Each specimen experiences the same loads in this configuration, but stress is determined by its gauge diameter. Therefore, each specimen deforms according to where it lies on its stress versus strain curve. This test has run entirely in 360°C simulated PWR primary water with 2000 ppm of boron, 2 ppm of lithium, and a dissolved hydrogen content of 25 cc/kg (corresponding to the Ni/NiO stability line).

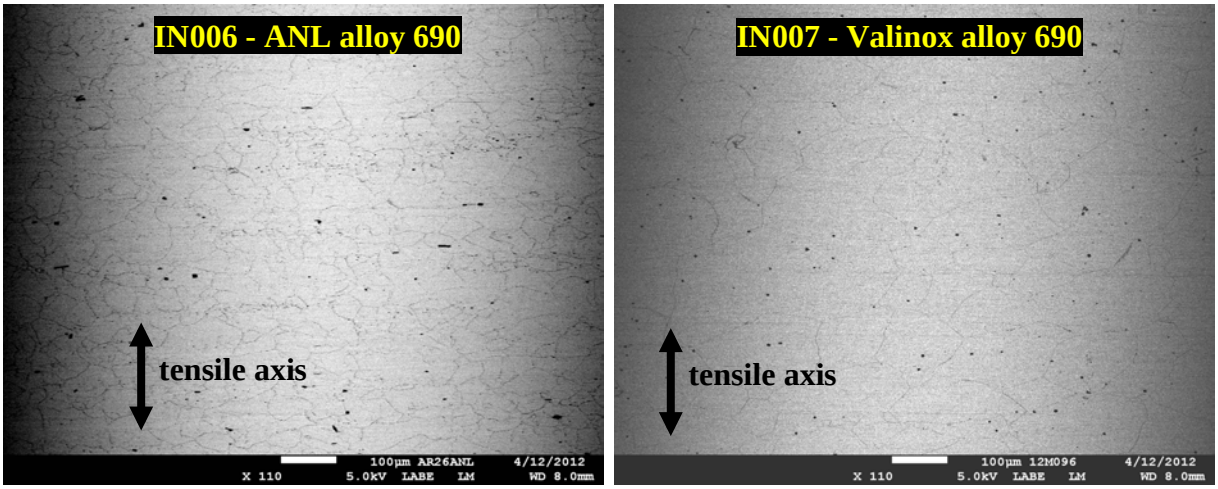

Figure 25. SEM backscatter images of a portion of the polished gauge section of IN006 and IN007 prior to testing revealing grain boundary carbides and TiN particles intersecting the specimen surface.

An overview of the test to-date is summarized in Figure 26. The specimen response is plotted as strain versus time using the referenced strain value as discussed in the experimental section. The stress level on the specimens is listed and "R&E" indicates that the specimens were removed and examined. The reference DCPD measurement primarily removes any phantom strains due to resistivity drift of the material, but it also partially removes elastic strains as well. The red line shows the outlet water conductivity of the autoclave and provides a measure of the water chemistry. Increases in stress were accomplished by constant displacement rate straining at $5x10^{-4}$ sec^{-1}. The test was started at 500 MPa (~70% of the initial 360°C yield strength for the specimens) and the detailed DCPD-based strain response during the first 1000 hours is presented in Figure 27. The peak-to-peak variability in the measurements is ~0.05% strain, and trends in the strain response can be identified down to approximately that same value. After 1000 hours, the specimens were removed for an initial examination. SEM backscatter images in Figure 28 show that the TiN particles in both materials had started to corrode. Neither specimen showed surface damage or cracks beyond that present in the CR materials prior to testing.

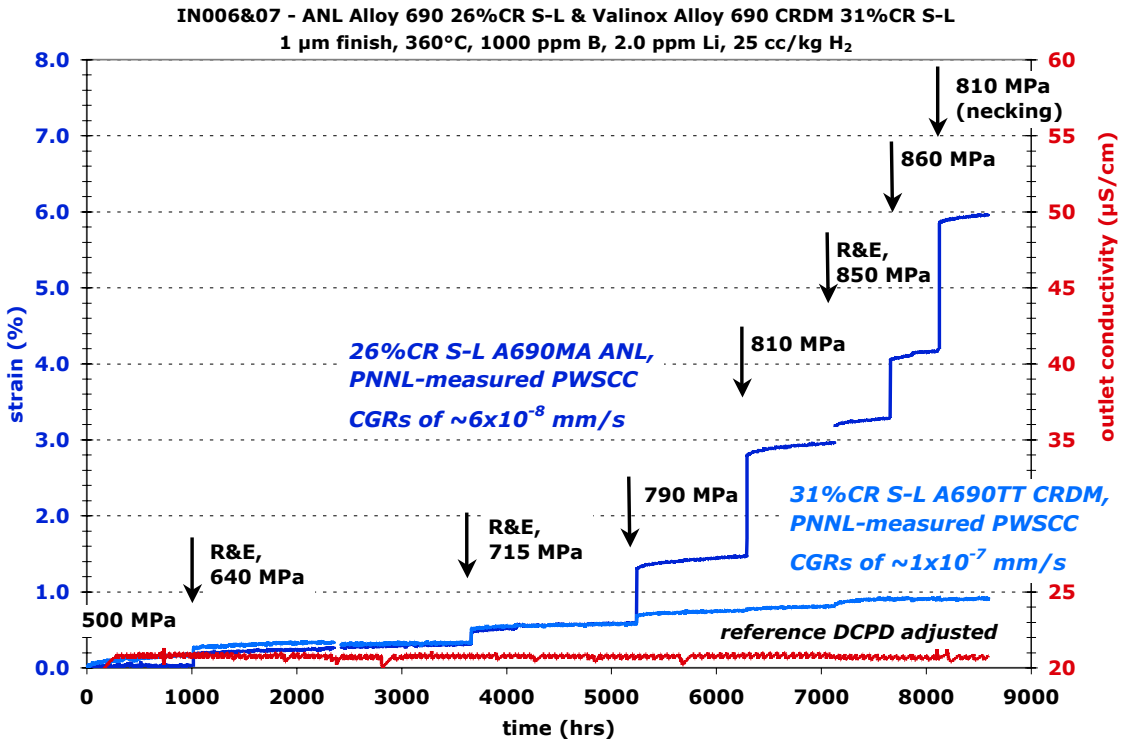

Figure 26. Overview of the test to-date on the two cold-rolled alloy 690 specimens, IN006 and IN007. Changes in stress on the specimens are listed. "R&E" indicates "remove and examine" the specimens.

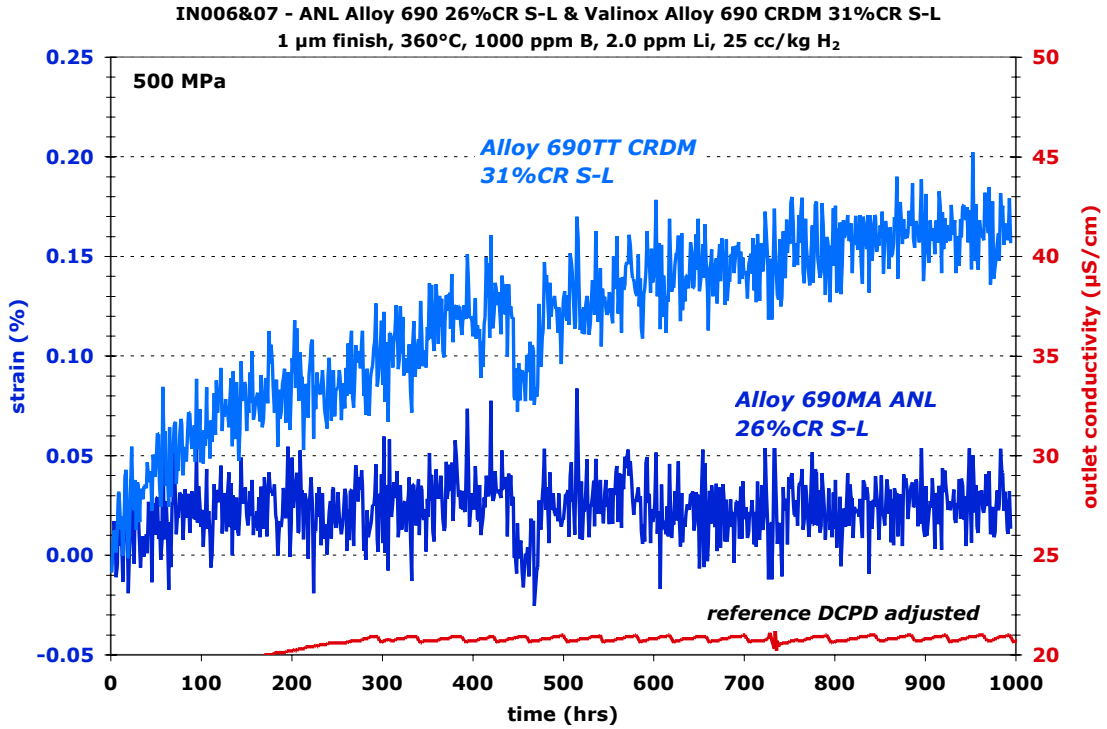

Figure 27. DCPD-based strain response of the two CR alloy 690 specimens, IN006 and IN007, during the first 1000 hours of testing.

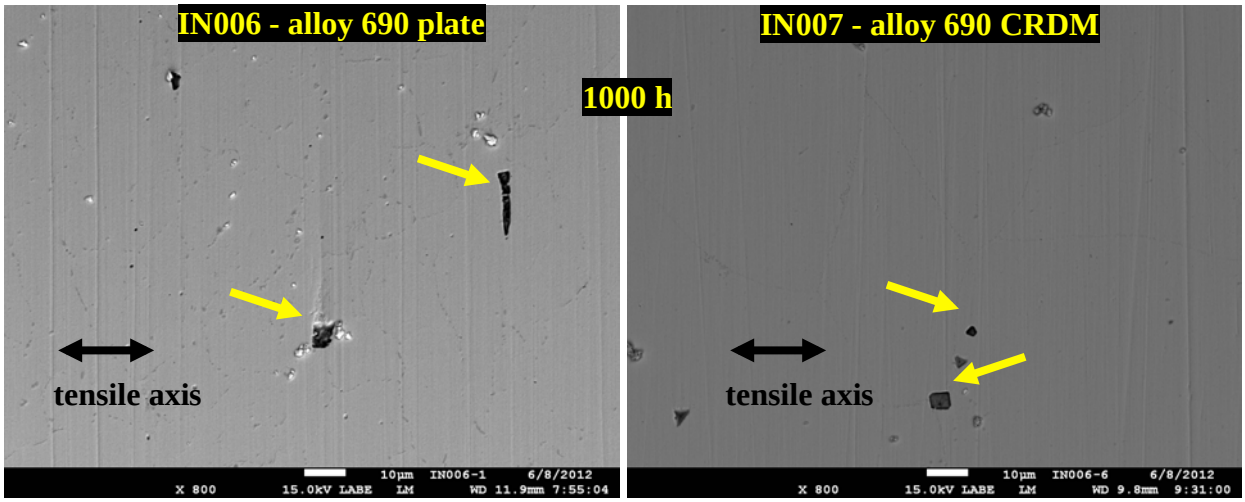

Figure 28. SEM backscatter images, respectively of the 26%CR plate and 31% CR CRDM specimen gauge sections revealing small grain boundary carbides and larger matrix TiN particles (identified by arrows) that have partially corroded.

The test was resumed at a stress of 640 MPa, or roughly 90% of the initial yield stress of the material. This stress level was maintained for 2600 hours as shown in Figure 29, at which point the specimens were again removed and examined. Analysis of the specimens revealed that most the TiN particles intersecting the surface were extensively corroded often leaving behind cavities. A key difference between the two materials was that small cracks were found associated with several corroded TiN stringers in the IN006 ANL plate material as shown in Figure 30(a). These cracks appeared to nucleate only off the longer TiN stringers (>15 µm) and the cracks were found to be from 2-10 µm long. They were predominantly TG, but cracks on or very near a grain boundary were occasionally observed as shown in Figure 31. No such cracks were detected off the corroded block-shaped TiN in the IN007 CRDM material (Figure 30b).

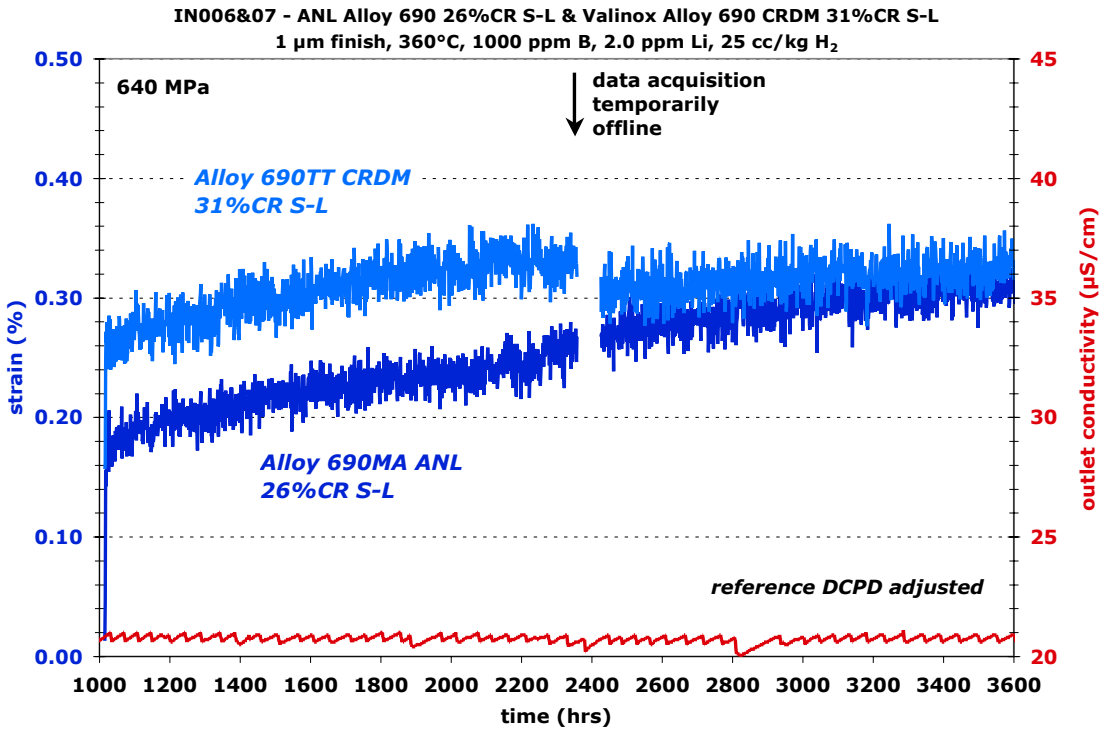

Figure 29. DCPD-based strain response of the two cold-rolled alloy 690 specimens (IN006 and IN007) from 1000 - 3600 hours.

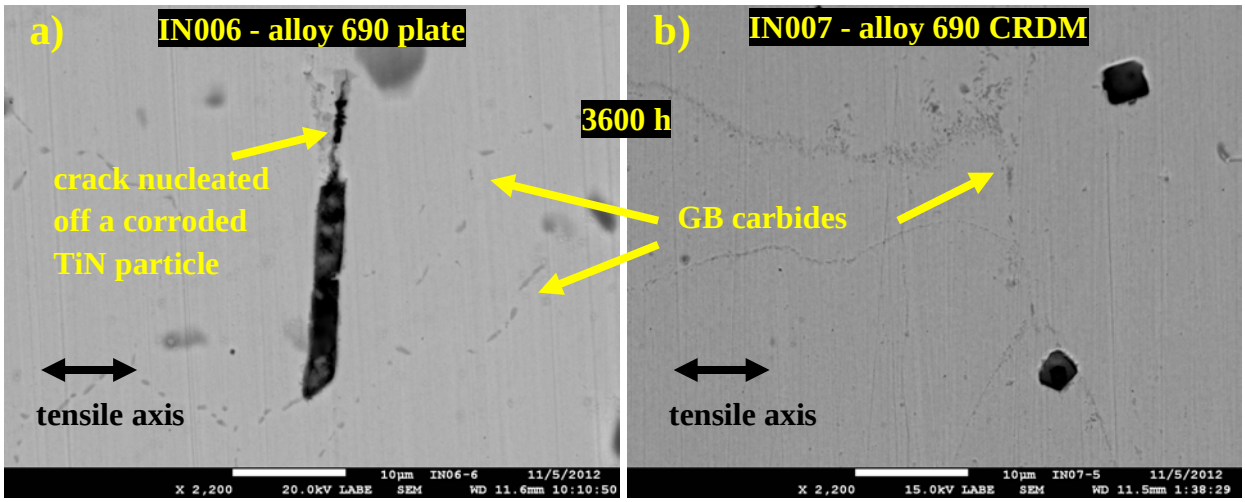

Figure 30. SEM backscatter images of the 26%CR plate and 31%CR CRDM specimens revealing grain boundary carbides and corroded TiN particles. Cracks nucleated from the ends of corroded TiN stringers were observed in the plate material while no cracking was observed in the CRDM material.

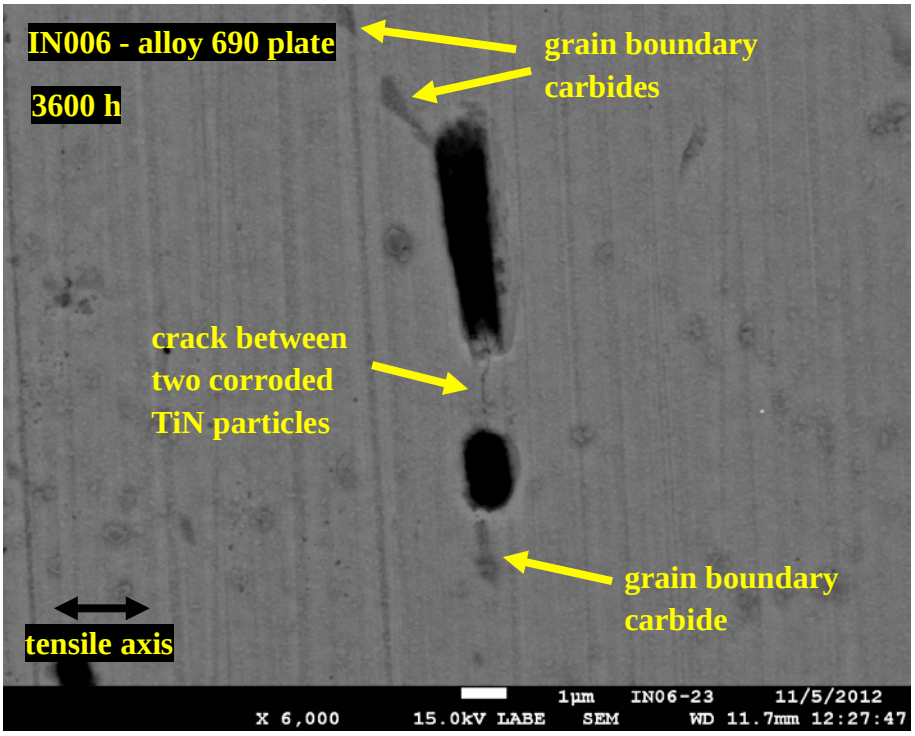

Figure 31. Crack between two corroded TiN particles that appears to be on a grain boundary in the 26%CR plate specimen IN006 after 3600 h.

The small cracks into the alloy 690 from the corroded TiN particles represent SCC initiation precursors and the test was resumed with anticipation that crack nucleation and growth would be detected by DCPD for the IN006 specimen in a relatively short period of time. Upon resuming the test at 3600 h, the load was increased until a small indication of plastic yield was observed in the reloading curve resulting in applied stress of 715 MPa. As shown in Figure 32, no DCPD indication of crack initiation was observed over a subsequent period of ~1700 hours. Since this test was meant to be a first scoping experiment to assess conditions for SCC nucleation in SCC-susceptible alloy 690 materials, the decision was made to further augment the crack initiation process by increasing the applied load and inducing additional plastic strain in the specimens. As tensile straining is performed with the specimens loaded in series, both specimens are subjected to the same loads but are not constrained to strain by the same amount. The 26%CR plate specimen IN006 that has a lower degree of cold work yielded first, underwent ~0.6% plastic strain and achieved a final stress of ~790 MPa as shown in Figure 33. The undulations in the plastic strain curve are thought to be due to dynamic strain aging that has also been observed in elevated temperature air tensile tests performed on these materials. The 31%CR CRDM specimen IN007 showed slight non-linear response, but did not undergo plastic deformation despite reaching nearly the same stress level.

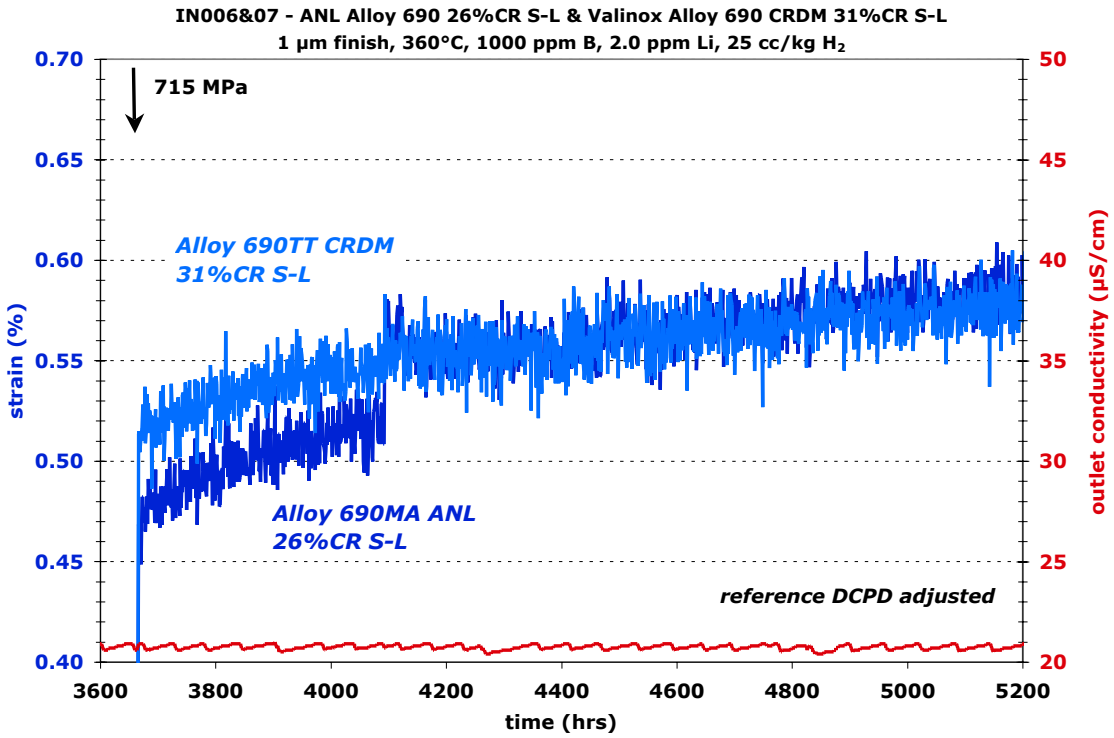

Figure 32. DCPD-based strain response of the two cold-rolled alloy 690 specimens (IN006 and IN007) from 3630 - 5200 hours.

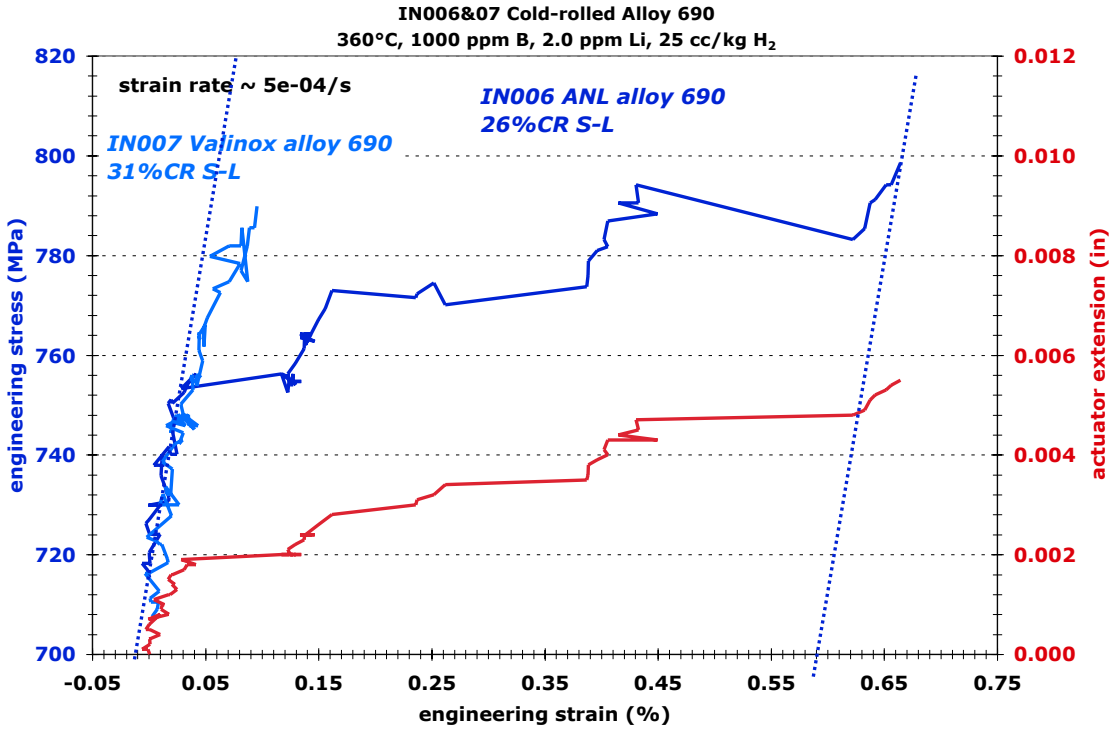

Figure 33. Tensile straining performed on the alloy 690 materials at ~5300 h. The 26%CR plate material (IN006) underwent approximately 0.6% plastic strain while the 31%CR CRDM material (IN007) did not yield.

After application of this more significant level of plastic strain in the 26%CR plate specimen that was observed to have cracks nucleated off corroded TiN stringers in the 3600-hour observation, there was a renewed expectation that measureable SCC crack initiation would occur quickly. However, once again no indication of SCC crack initiation was detected during the following ~1000-hour exposure under constant load at the yield stress as documented in Figure 34. Slow straining was again applied as shown in Figure 35. The 26%CR plate specimen IN006 underwent an additional ~1.2% plastic strain, while the 31%CR CRDM specimen IN007 did not yield. In the prior straining events, the 26%CR plate specimen underwent a slight amount of strain hardening but this time the specimen exhibited an overall flat plastic strain curve indicating that geometric instability (necking) could begin during any subsequent straining. Despite the overall flat strain hardening response, a slight increase in stress was achieved by stopping the straining process at a peak in a strain serration.

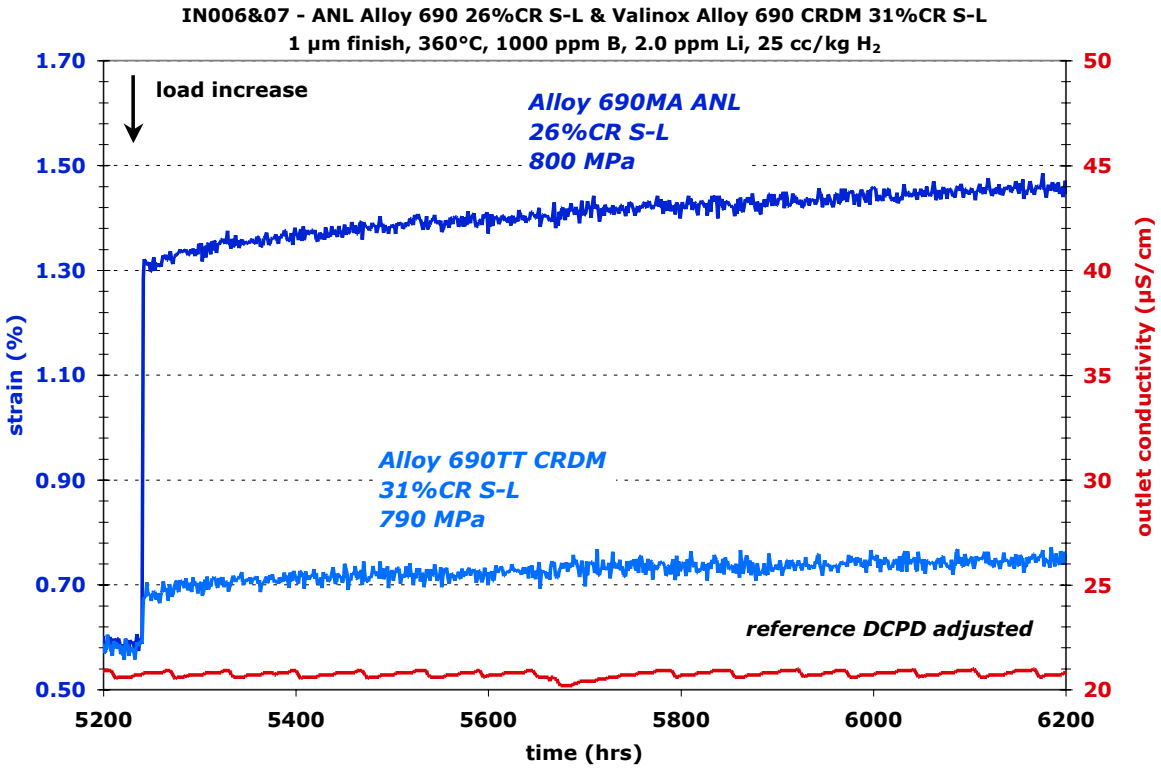

Figure 34. DCPD-based strain response of the two cold-rolled alloy 690 specimens (IN006 and IN007) from 5220 to 6200 hours.

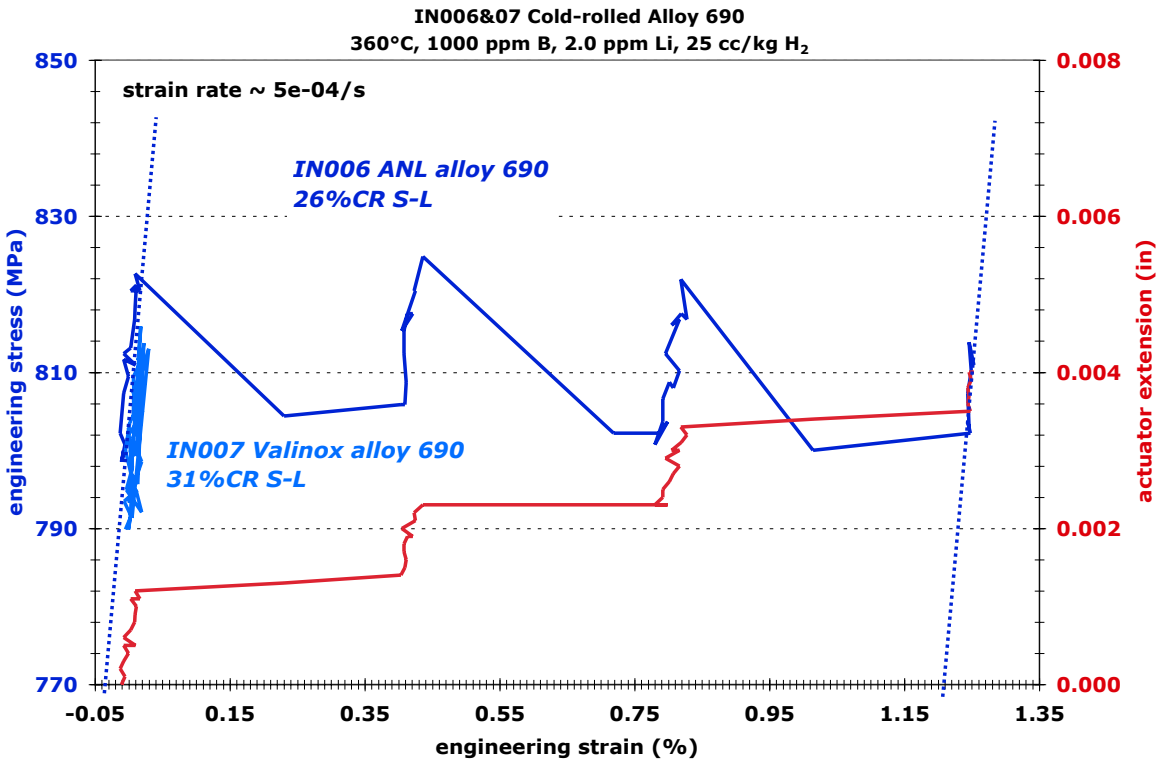

Figure 35. Tensile straining performed on the alloy 690 materials. The 26%CR plate material (IN006) underwent approximately 1.2% plastic strain while the 31%CR CRDM material (IN007) did not yield.

After ~800 hours went by with no indication of SCC crack initiation (Figure 36), the decision was made to interrupt the test (at ~7100 hours) for another round of specimen examinations. The surface appearance of the 31%CR CRDM specimen IN007 had not noticeably changed. However, the 26%CR plate specimen IN006 exhibited a higher density of small cracks associated with the corroded TiN particles, had more cracks that appeared to be IG and crack openings were larger as illustrated in Figures 37 and 38. Another important difference was that there were obvious surface strains in the specimen, and a reasonably clear example is presented in Figure 39. A much higher density of Ni-Fe spinels were found on the specimen compared to the previous observation at 3600 hours. Figure 40 shows that the spinels were often decorating cracks or surface strained regions. Further surveys of the surface revealed that crack lengths were now more frequently in the 10 μm range and crack openings were often ~1 μm, even though there had been no obvious in-situ indication of crack initiation by DCPD.

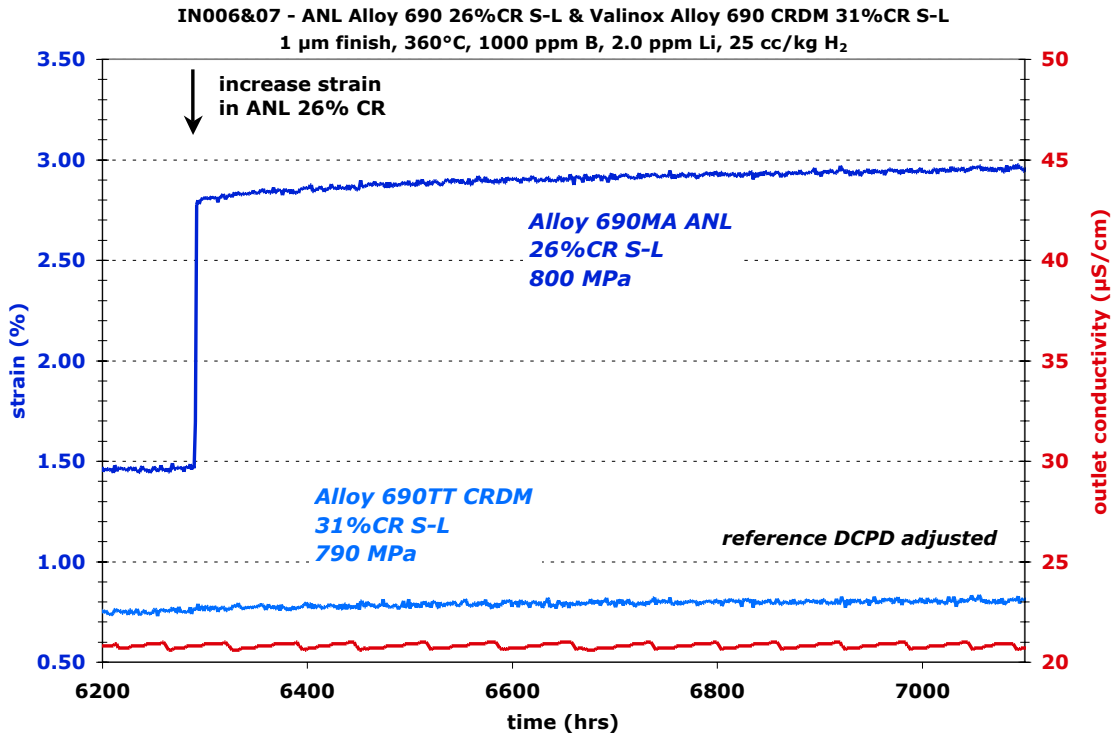

Figure 36. DCPD-based strain response of the two cold-rolled alloy 690 specimens (IN006 and IN007) from 6200 - 7100 hours.

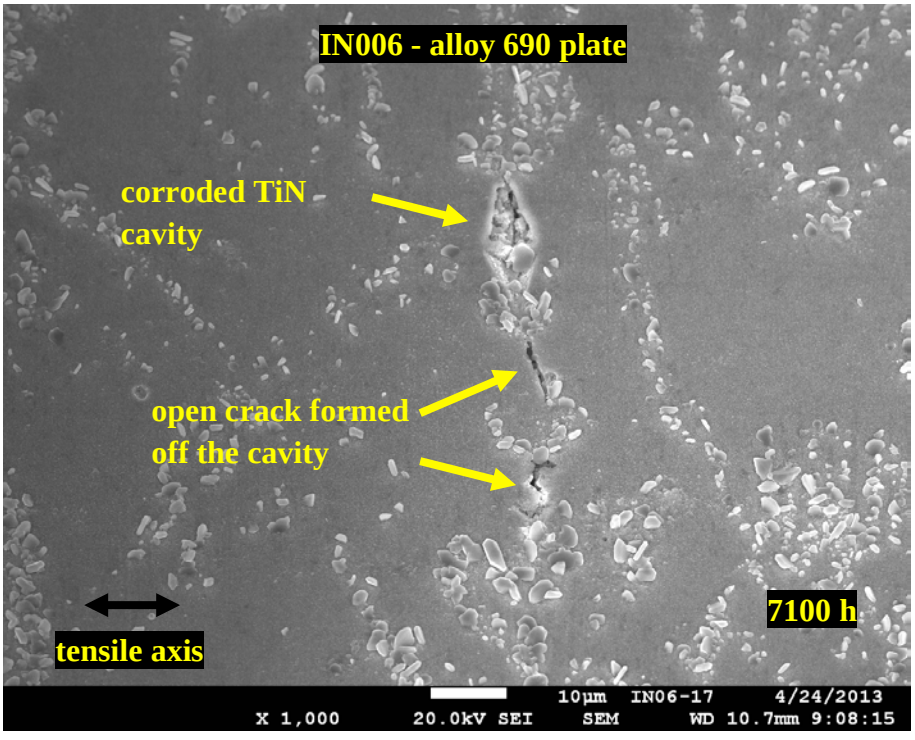

Figure 37. Example of surface crack morphology in the 26%CR plate specimen (IN006) after ~7100 hours of exposure.

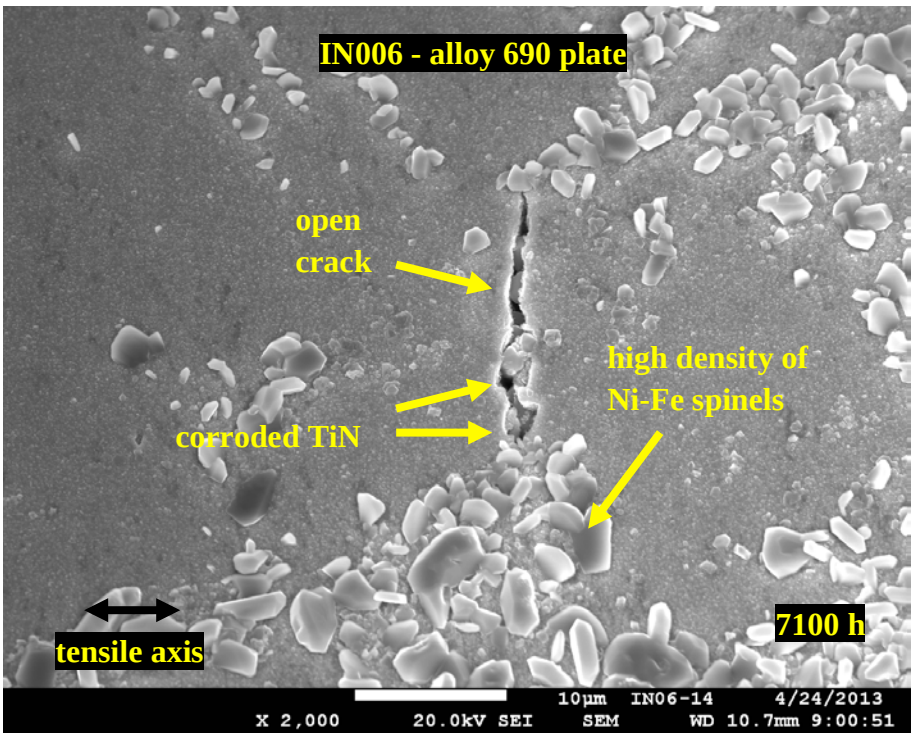

Figure 38. Example of surface crack morphology in the 26%CR plate specimen (IN006) after ~7100 hours of exposure.

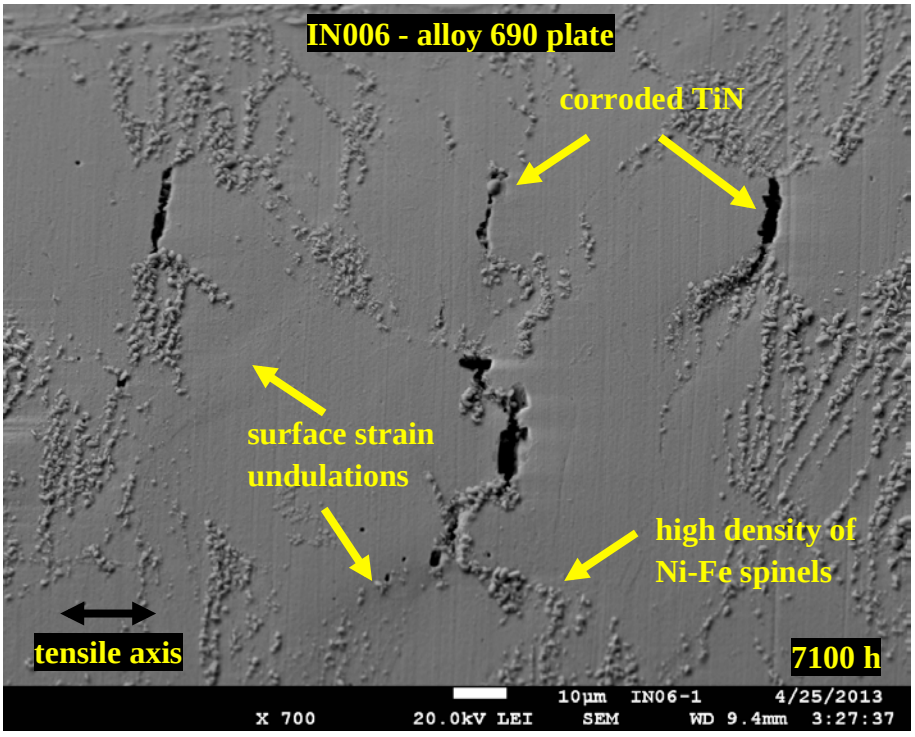

Figure 39. Observable surface strains on the 26%CR plate specimen (IN006) after ~7100 hours of exposure. Surface strains were often obscured by Ni-Fe spinels.

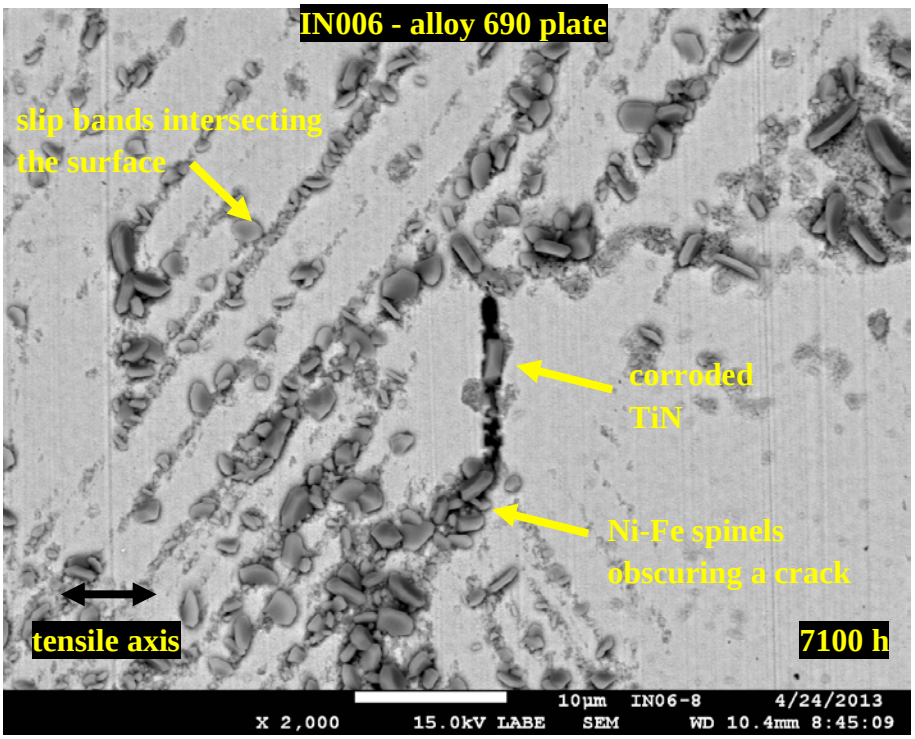

Figure 40. Ni-Fe spinels located on what appear to be twin boundaries and a crack nucleated off a corroded TiN particle on the 26%CR plate specimen (IN006) after ~7100 hours of exposure.

While cross-section examinations of unstressed alloy 690 surface exposure specimens had shown a protective Cr_2O_3 film above grain boundaries intersecting the surface, no information was available on what was occurring below the surface of exposed grain boundaries in the alloy 690 specimens under stress. In order to obtain initial information on the small IG surface cracks formed in the IN006 specimen, a FIB was used to form trenches into the specimens to expose selected subsurface cracks in cross section. Figure 41 shows a step-by-step example of the trenching process where an IG crack nucleated off a corroded TiN stringer is revealed. With a resulting size of ~5 µm in all dimensions, the trench is in the same size range as the TiN particles and is not expected to have any significant effect on the crack initiation behavior.

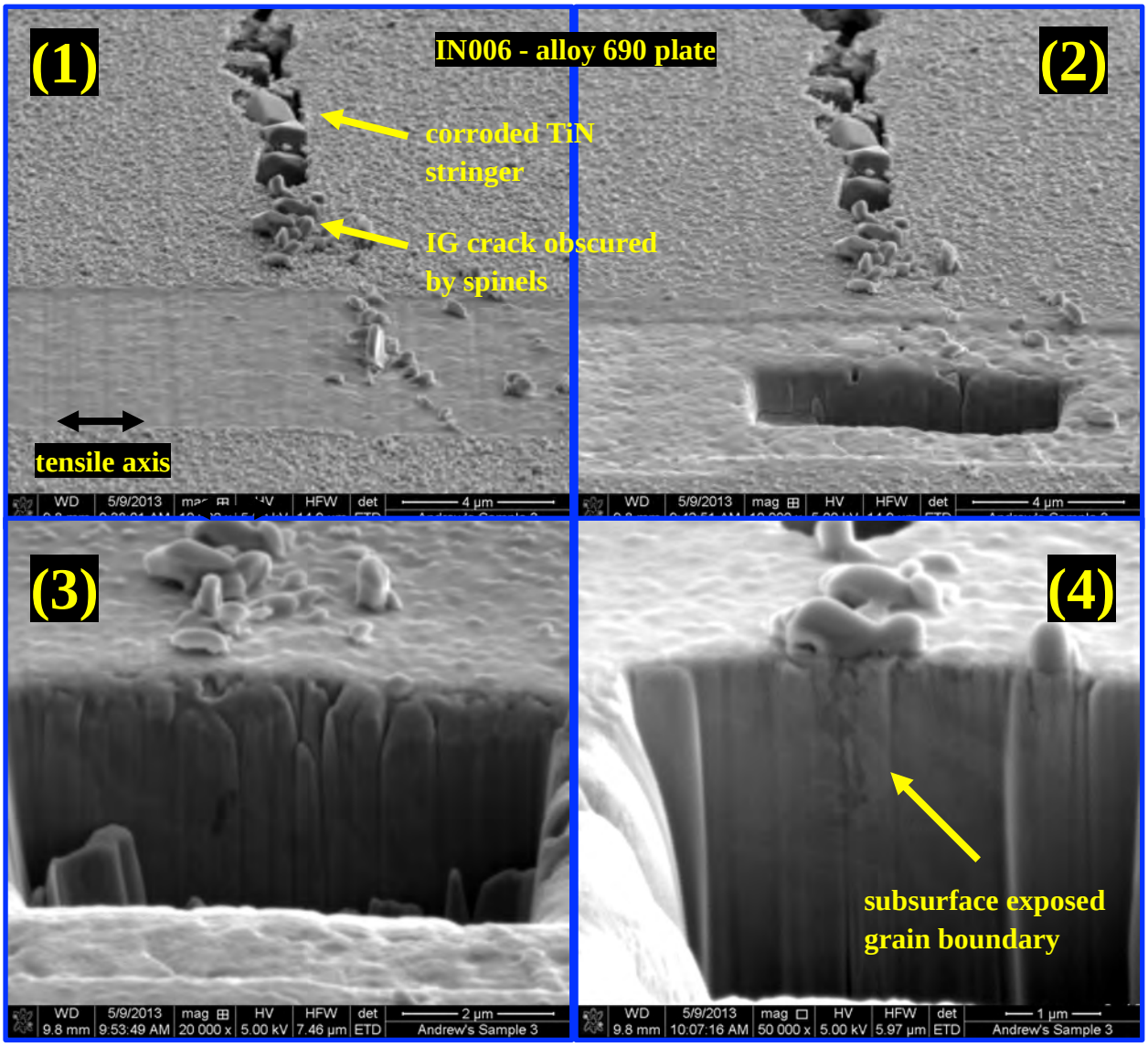

Figure 41. Step-by-step imaging of the formation of a trench into the surface of the 26%CR plate specimens (IN006) to reveal a subsurface IG crack in cross section.

As discussed previously, a small fraction of the TiN particles were coincident with grain boundaries, and in several cases, the cracks that nucleated off these corroded particles were IG. The FIB trench process was used to view these types of cracks with two examples shown in Figures 42 and 43. These cracks were verified to be IG by the presence of semi-continuous carbides that are only found on grain boundaries in this material. The cracks were limited to a rather shallow depth of 1-2 µm, and crack wall penetrative oxidation (commonly seen in alloy 690) was observed in both specimens. The extent of attack off crack walls suggests that the IG crack extension may have formed during the dynamic straining event at 6300 hours and no further IGSCC growth occurred under constant load from 6300 to 7100 hours. More detailed examinations of cracks using this method are planned at the conclusion of the test.

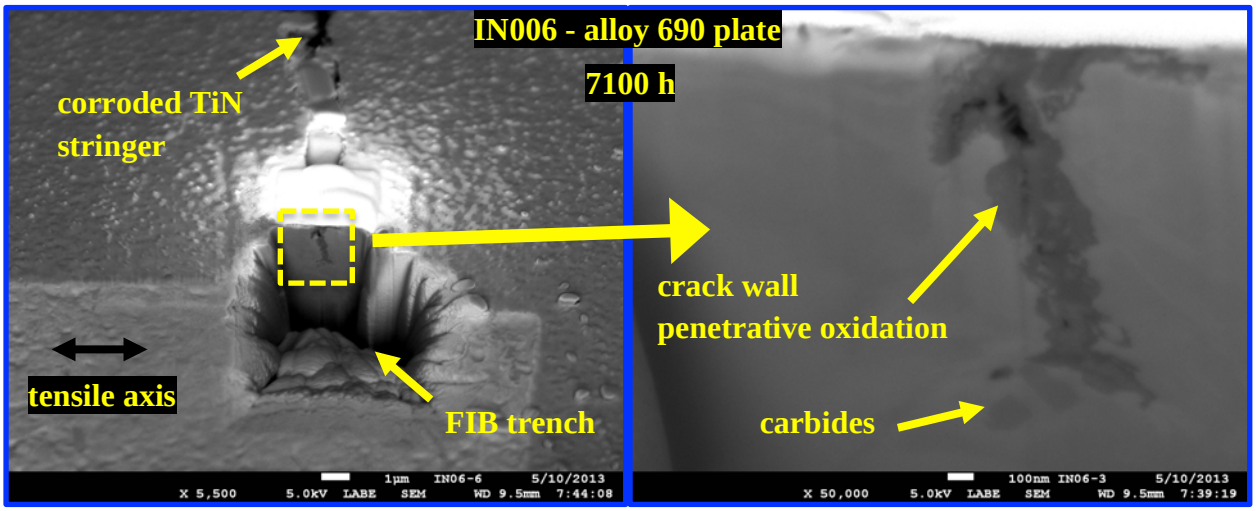

Figure 42. Strain driven IG crack in the 26%CR plate specimen as viewed in cross section using the FIB trench process. Cracking was limited to a depth of ~1 µm.

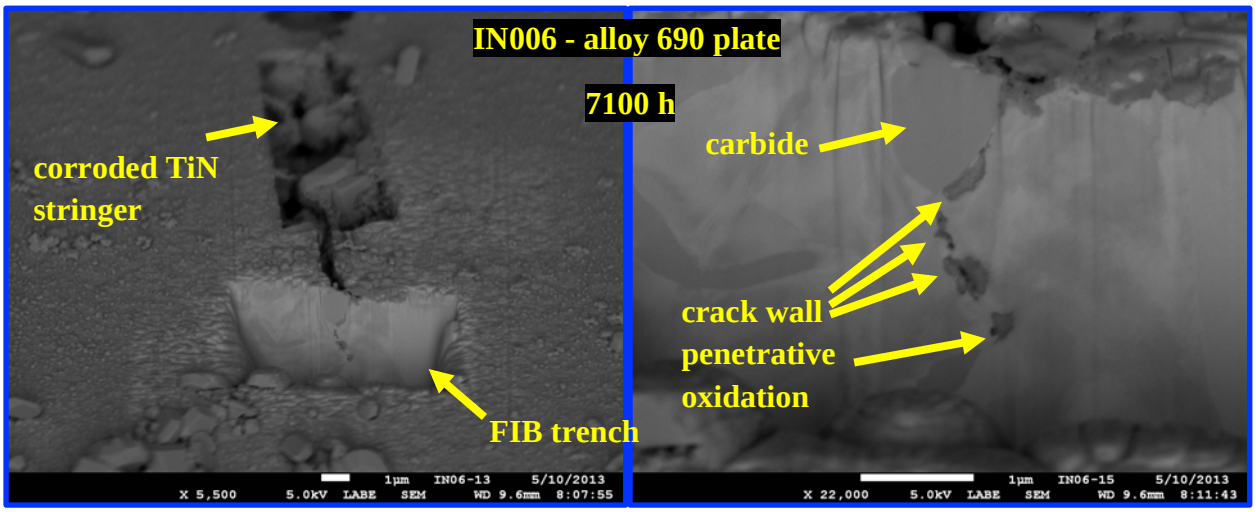

Figure 43. Second example of a strain driven IG crack in the 26%CR plate specimen as viewed in cross section using the FIB trench process. Cracking was limited to a depth of ~2 µm.

These small IG cracks represent likely precursors for IGSCC nucleation in the smooth surface specimens. However with no clear indication of a transition to IGSCC by either DCPD or SEM observations, the specimens were again reloaded into the crack initiation test systems for further exposure. An additional ~0.2% plastic straining was applied to ensure that the specimens were at the maximum possible load. Surprisingly, it was possible to increase the load slightly to produce an applied stress of ~850 MPa for the specimens, a value that is beyond the ~750-780 MPa ultimate tensile strength of the 26%CR alloy 690 plate material in the CR condition. This increased strength is due to an as-yet unidentified, aging-induced microstructural change at 360°C and may be linked to the increase in resistivity for these alloy 690 materials. Detailed

assessments of the alloy microstructures and microchemistries will be made to understand the origin of the strength increase when the test is ended.

After ~500 hours (to ~7600 h total test time) at 850 MPa with no indication of crack initiation, the 26%CR plate specimen IN006 was plastically strained an additional ~0.8% (Figure 44), bringing the total plastic strain up to ~4%. The yield point again increased to ~890 MPa, but then the stress decreased slightly to ~870 MPa with a concurrent flat plastic response that reinforced that the specimen was close to necking. In order to avoid runaway straining during constant load, the stress was dropped slightly to 860 MPa. When no initiation was observed from ~7650 hours to ~8100 hours as shown in Figures 45 and 46 for the 26%CR plate and 31%CR CRDM specimens, respectively, a final ~1.7% plastic strain was added to the 26%CR alloy 690 plate, bringing the total strain up to ~6%. The stress after straining dropped to ~810 MPa due to a more significant reduction in load carrying capacity that occurred during this straining event. Another 800 hours has been accumulated as illustrated in Figures 46 and 47, and the test continues to run without any indication of crack initiation by in-situ DCPD. The test will be ended shortly with a total test time of ~9100 hours (>1 year) if crack initiation does not occur before that time. Detailed SEM characterizations of the gauge surfaces will subsequently be performed on both specimens. The 26%CR plate specimen IN006 will then be cross sectioned, and systematic examinations of IG cracks will be conducted. After the surface SEM examinations, the decision will be made whether to do the same on the 31%CR CRDM specimen IN007 or reload the specimen to further evaluate dynamic straining (note that this specimen was not plastic strained during the periodic load increases).

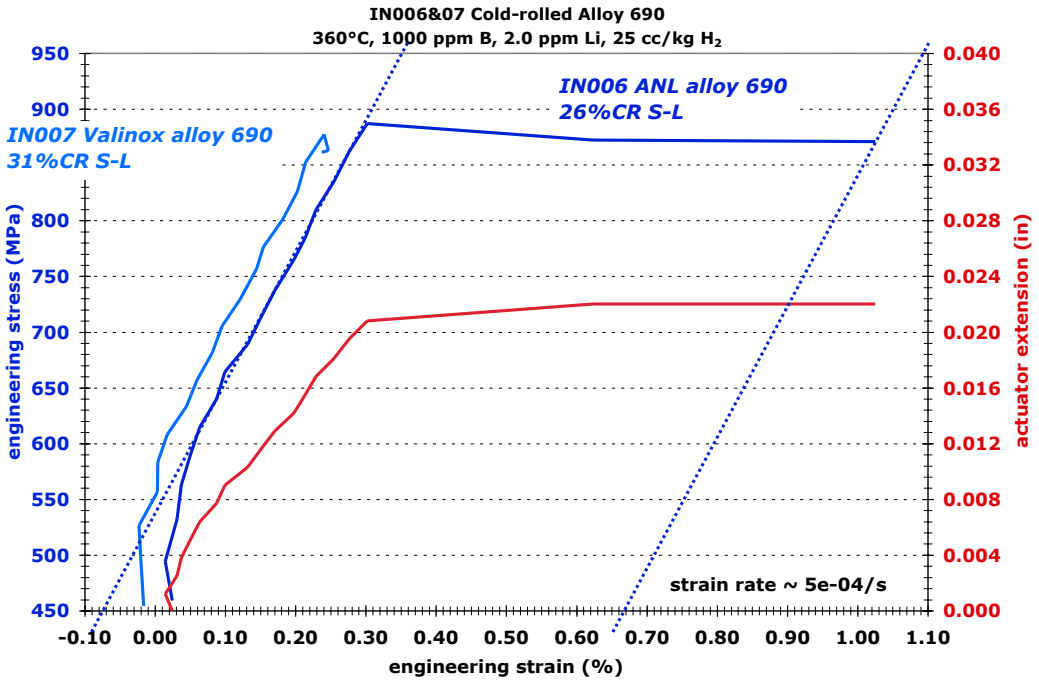

Figure 44. Plastic strain applied to the 26%CR ANL alloy 690 plate specimen IN006 at ~7600 h.

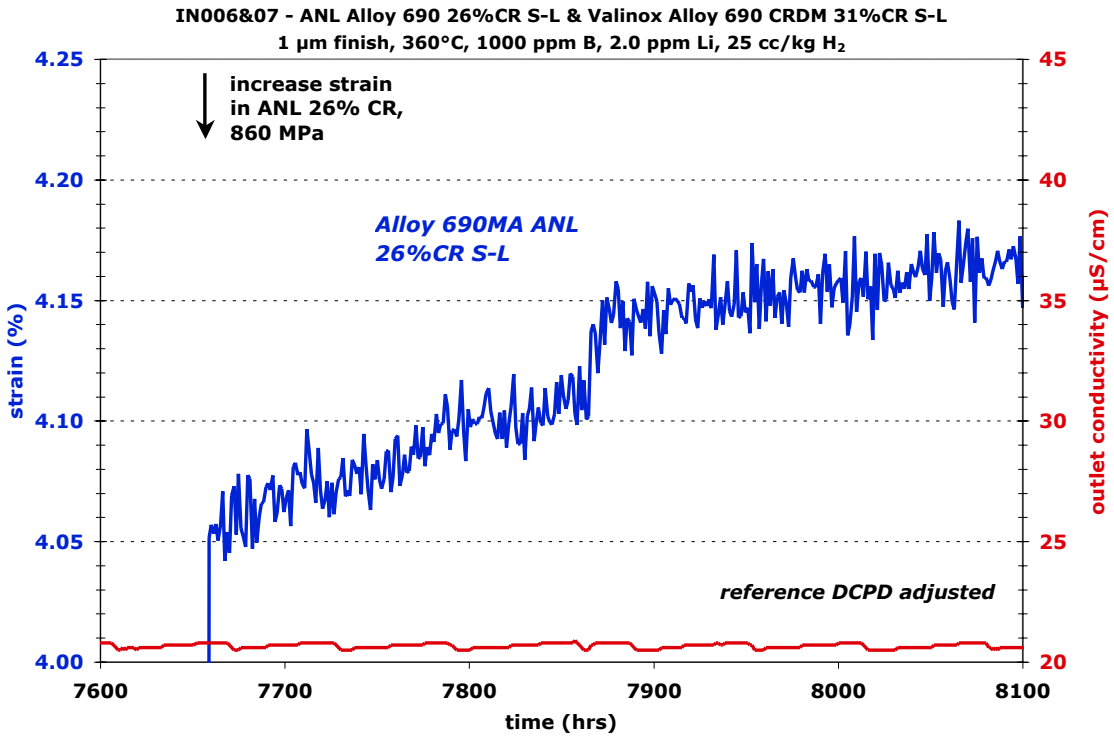

Figure 45. DCPD-based strain response of the 26%CR ANL alloy 690 plate specimen IN006 from 7650 to 8100 hours.

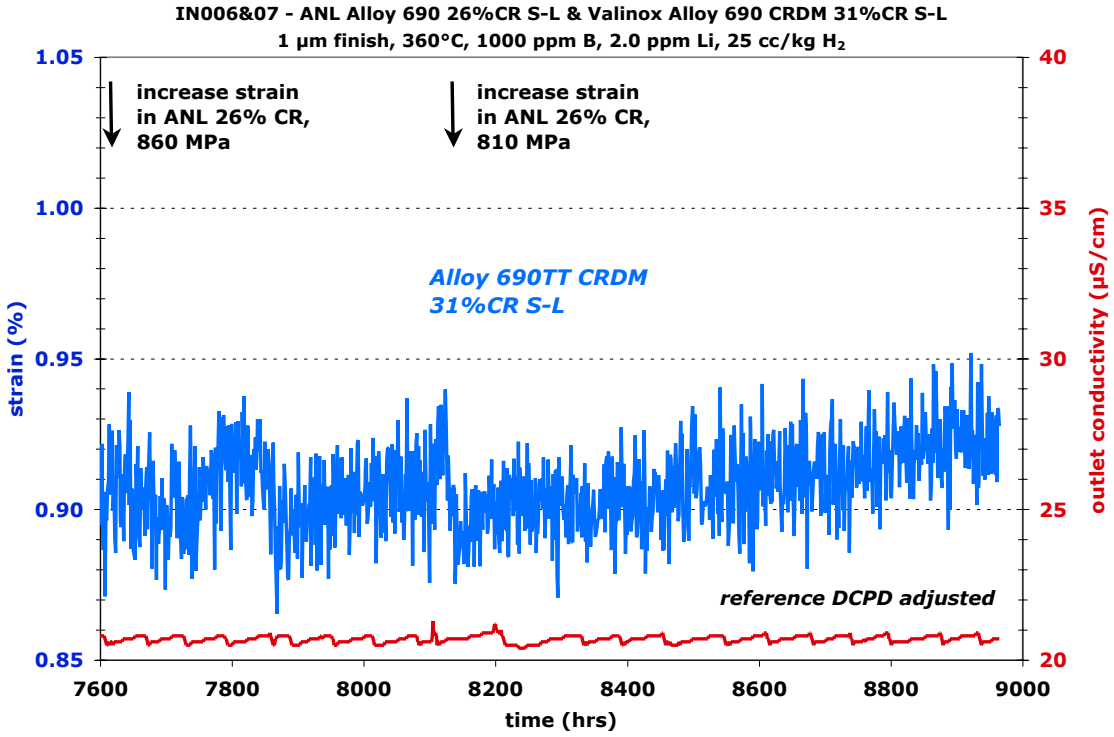

Figure 46. DCPD-based strain response of the 31%CR alloy 690 CRDM specimen IN007 from 7600 to 8950 hours.

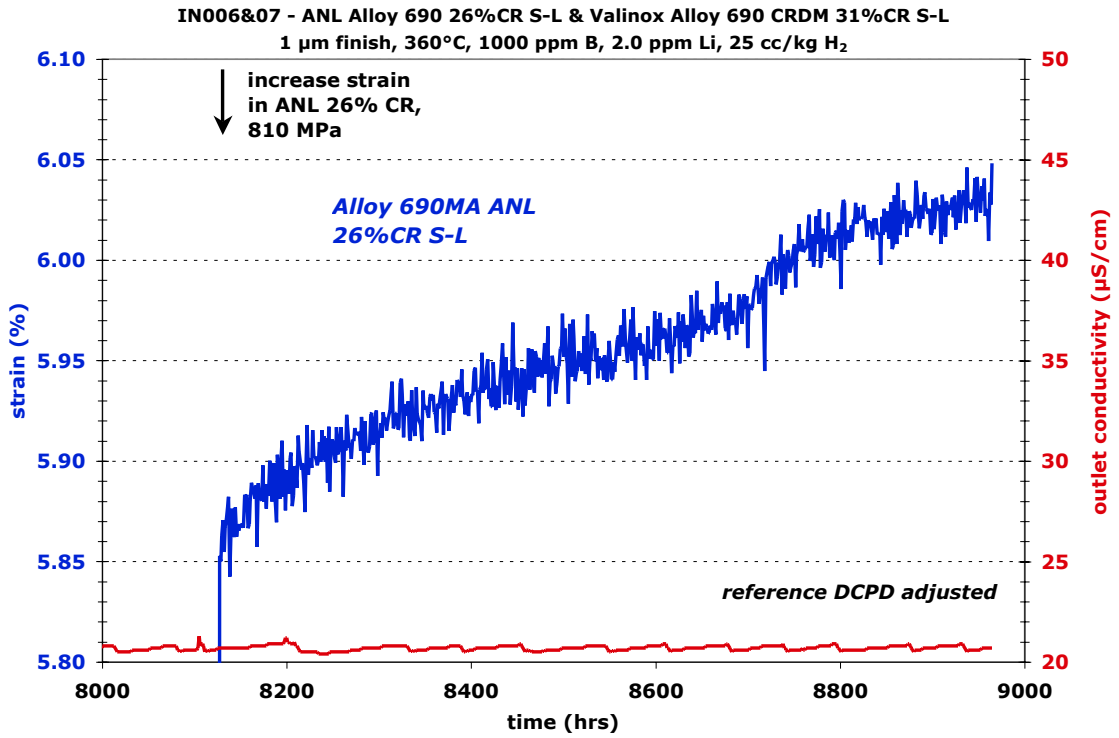

Figure 47. DCPD-based strain response of the 26%CR ANL alloy 690 plate specimen IN006 from 8150 to 8950 hours.

SCC Initiation Test Results on Tensile Strained Alloy 690 (IN009-IN012)

Four scoping tests were performed on tensile-strained alloy 690 materials. IN009 was made from alloy 690 billet originally purchased by GE (heat B25K), while IN010 was made from the ANL alloy 690 plate (the same heat as used for the IN006 cold-rolled specimen discussed above). Both specimens were cold tensile strained to ~18% plastic strain, and then the gauge sections were polished to a 1 µm finish prior to testing at 360°C. At about 350 hours into the test, adverse weather resulted in a lightning strike that caused an uncontrolled power spike that forced the test system to overload the specimens. The IN009 specimen made from the GE alloy 690 was strained an additional ~4%, and the IN010 ANL alloy 690 plate specimen was strained an additional ~12%. The specimens were removed from the test system for examination, and while both were still in good condition (no necking or other unusual features), this shutdown was used as an opportunity to exchange the GE specimen for a specimen made from the same 31%CR CRDM material as specimen (IN007). In addition, the decision was made to increase the tensile strain and attempt to match the measured initial yield strengths for the CR IN006 and IN007 specimens. The new CRDM specimen (IN011) was cold tensile strained to 41% plastic strain, while the alloy 690 plate specimen (IN010) was cold strained to a total tensile plastic strain up to 31%.

These two specimens, again with a 1 µm diamond polish on the gauge section, were tested at constant load at 360°C. During the initial loading, the alloy 690 CRDM specimen IN011 was

allowed to undergo ~1% plastic strain in an attempt to reach the yield stress in the ANL alloy 690 plate specimen IN010. However, the stress versus strain plot for the CRDM specimen showed a slightly negative slope during plastic straining indicating that necking may have already begun. Load was adjusted to prevent the specimen from undergoing in-situ straining failure, and after ~1400 hours of exposure as shown in Figure 48, the test was stopped to examine the specimens. SEM-based examinations in unstrained regions of the surface revealed that TiN particles were corroded as observed in IN006 and IN007, but no cracks into the alloy 690 were found. In the necked region of the 41% tensile strained alloy 690 CRDM, significant strains were observed on the surface as shown in Figure 49. Small TG cracks were observed to have nucleated from some of the corroded TiN particles as illustrated in Figure 49(d) and in Figure 50.

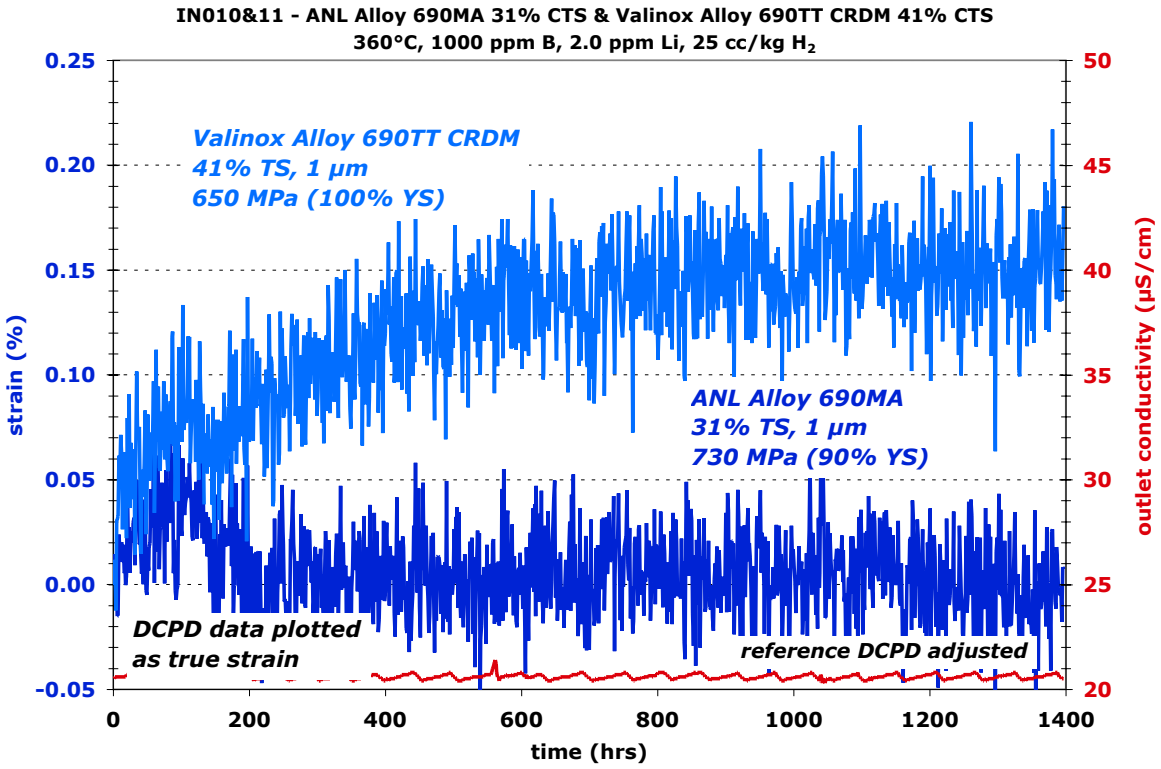

Figure 48. 31% tensile strained ANL alloy 690 plate (IN010) and 41% tensile strained alloy 690 CRDM (IN011) response during exposure in 360°C simulated PWR primary water at constant load near the yield stress.

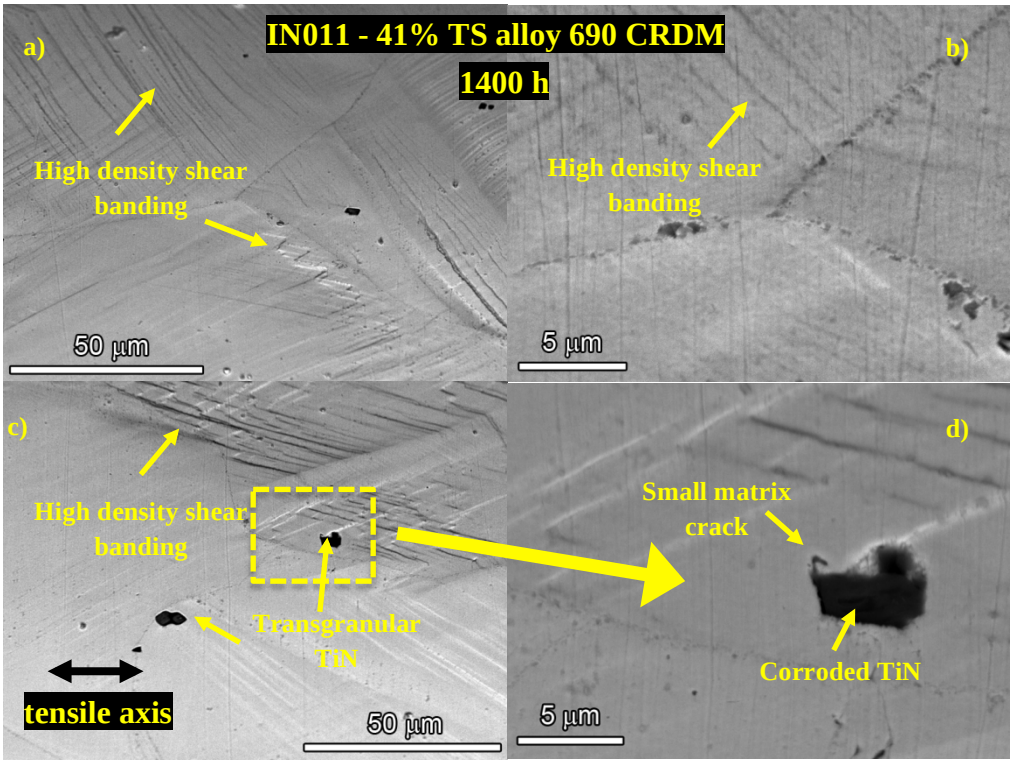

Figure 49. SEM-BSE images of the surface of 41% tensile strained alloy 690 CRDM specimen IN011 showing high levels of shear banding. No apparent IG crack initiation was observed. Representative grain structures are shown in a) and b). Corrosion and cracking of TG TiN particles was observed (c-d).

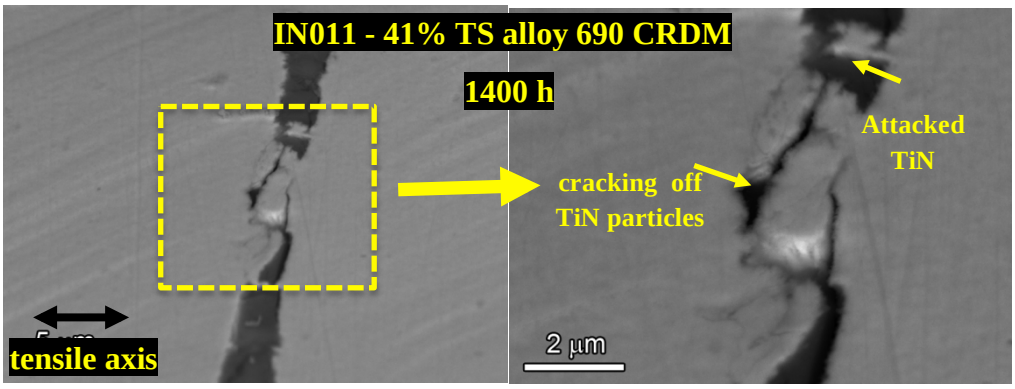

Figure 50. SEM-BSE images of the surface of 41% tensile strained alloy 690 CRDM specimen IN011. Corrosion and cracking of TG TiN particles was observed.

The decision was made to discontinue the test on the 41% tensile strained specimen and it was metallographically prepared in cross section to allow characterizations of damage microstructures. The in-situ plastic strain introduced into the specimen did result in surface damage near grain boundaries as illustrated in Figure 51 where a small V-shaped crack is observed to have formed. No evidence for grain boundary corrosion near or at the surface was observed, and instead a thin Cr_2O_3 film was found above grain boundaries intersecting the surface as shown in Figure 52, consistent with observations of unstressed specimens discussed earlier in this report. Void formation observed throughout material adjacent to carbides was due to the initial 41% cold-tensile straining and there was no indication that the void density or size increased during the initiation test at 360°C.

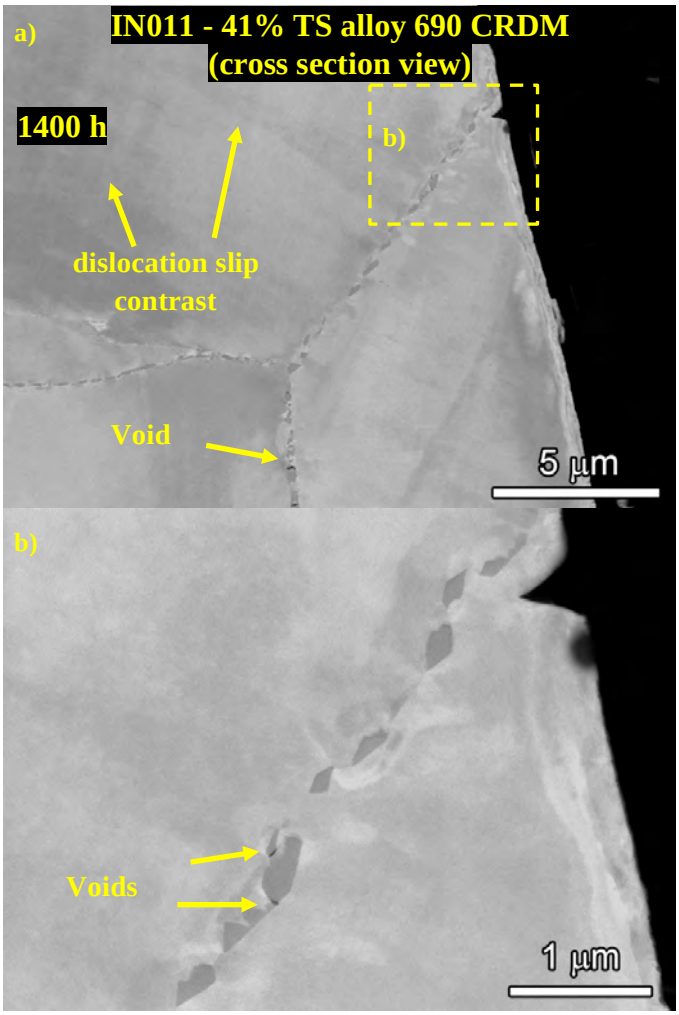

Figure 51. These cross section images illustrate deformation seen close to a grain boundary intersecting the surface of the specimen. The V-shaped feature is likely a result of a slip band. Void formation adjacent to carbides as shown here was seen throughout the necked region, including in the bulk away from the surface. No evidence for localized grain boundary corrosion or oxidation is seen.

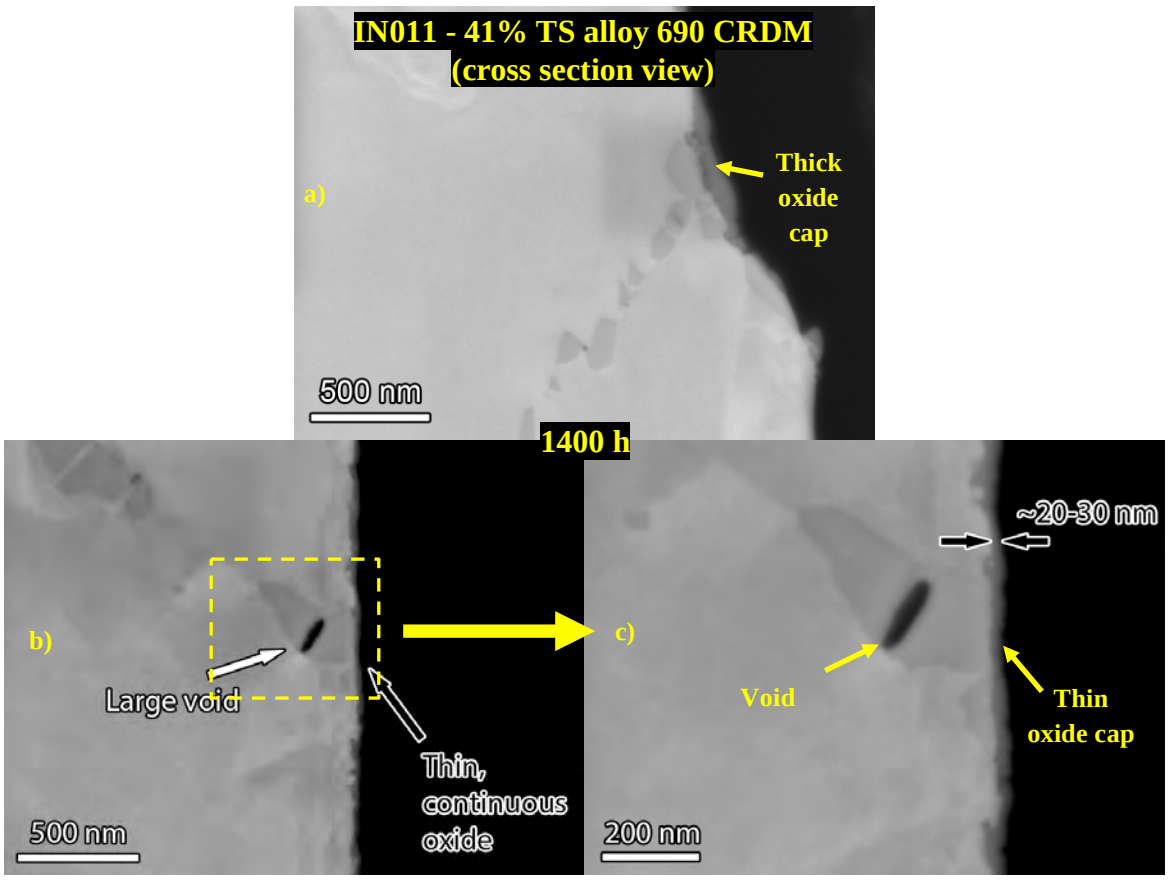

Figure 52. SEM-BSE images of the 41% tensile strained alloy 690 CRDM illustrating a thin, 20-30 nm, continuous oxide at the surface and voids between IG carbides.

A third exposure on tensile strained material followed and consisted of pairing the 31% tensile strained, ANL alloy 690 plate specimen (IN010) having 1400 hour of prior exposure with a new alloy 690 CRDM specimen of the same heat (IN012), this time with the specimen plastically strained to 24%. Knowing that IN012 was going to have a lower strength than IN010 due to a lower degree of cold work, the gauge diameter of IN010 was made slightly larger so that the yield load would be similar. An overview of the entire test is shown in Figure 53. As with the test on the CR specimens (IN006/IN007), periodic load and strain increases were applied as indicated in the plot, however two additional loading schemes were also employed. From ~1200 to ~1700 hours, a 0.001 Hz cycle with R = 0.5 was applied every 10 hours. This produced no observable change in the specimen response, and at ~1700 hours, the load cycle was removed and followed by slowly increasing the load (stress) that induced a small amount of plastic strain. In this instance, the alloy 690 CRDM specimen IN012 underwent ~1.5% plastic strain while the ANL alloy 690 plate specimen IN010 underwent ~0.2% plastic strain. After another 1000 hours with no indication of crack initiation, the load was again increased to induce additional plastic strain. This time it was the ANL alloy 690 plate specimen that underwent significant plastic strain while the alloy 690 CRDM specimen IN012 did not plastically strain at all.

As this test was reaching ~3000 hours of exposure, the test on the CR specimens (IN006/IN007) reached ~6300 hours of exposure with no indication of crack initiation. With a strong likelihood that the application of periodic plastic strain would not sufficiently accelerate the crack initiation process for the IN010/IN012 specimens, the decision was made to apply continuous slow straining. At ~3200 h, loading was converted to constant extension rate at 2.6×10^{-8} in/sec at the actuator. Neglecting load-train stretch (it is small under these conditions of low strain hardening) and assuming that the extension is evenly distributed between the two specimens, this produces a gauge strain rate of ~1×10^{-7} s^{-1}, within the typical range often used for slow strain rate SCC experiments.

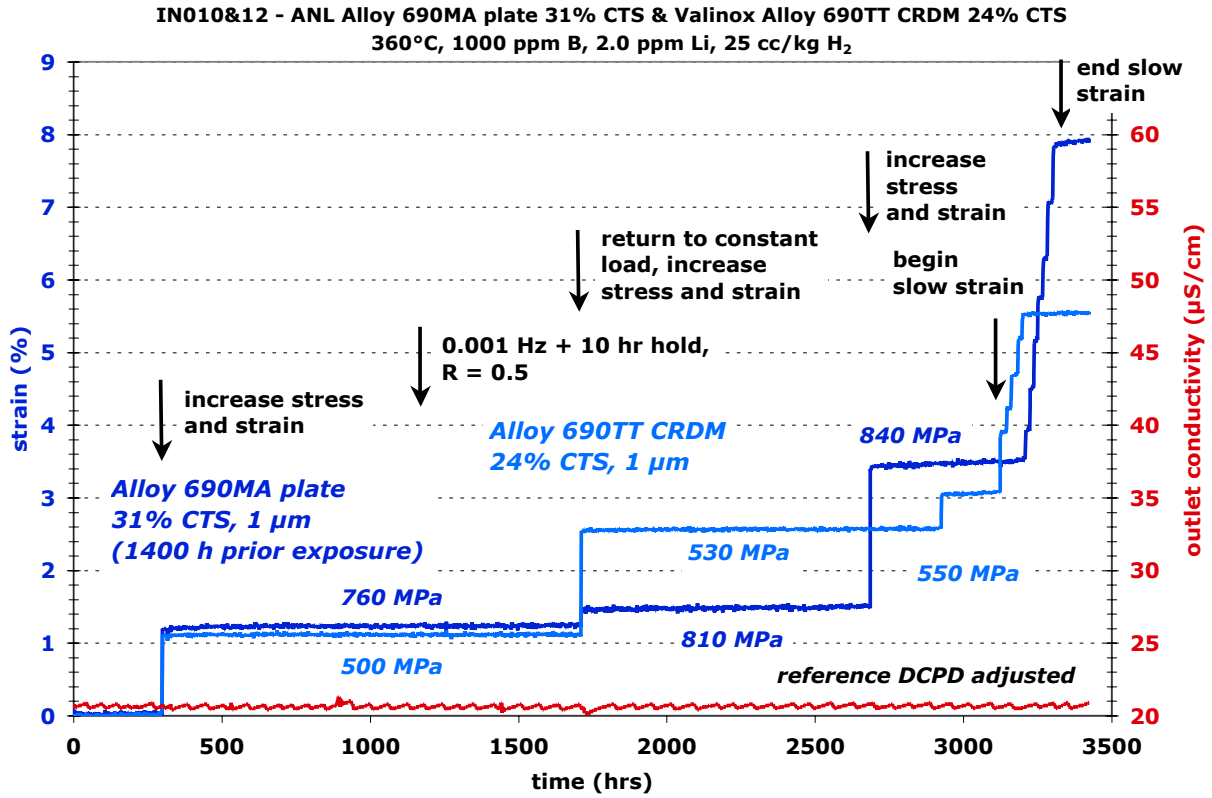

Figure 53. Overview of the entire test on the 31% tensile strained alloy 690 plate (IN010) combined with a 24% cold tensile strained alloy 690 CRDM specimen (IN012). Note that IN010 has 1400 hours of prior exposure.

Figure 54 shows this portion of the test in greater detail and includes the actuator displacement data. The steps in the strain plots are due to a combination of load train elasticity, friction between the pullrod and the pullrod environmental seal, and probably dynamic strain aging. As can be seen, the 24% cold tensile strained alloy 690 CRDM specimen IN012 underwent ~2.5% plastic strain before it sufficiently strain hardened to drive the 31% cold tensile strained alloy 690 plate to start plastically straining. At this point, all additional extension was absorbed only by the plate specimen, and upon reaching ~4.5% plastic strain after a period of ~200 hours, the test was converted back to constant load. The test was then ended ~100 hours later to perform specimen examinations.

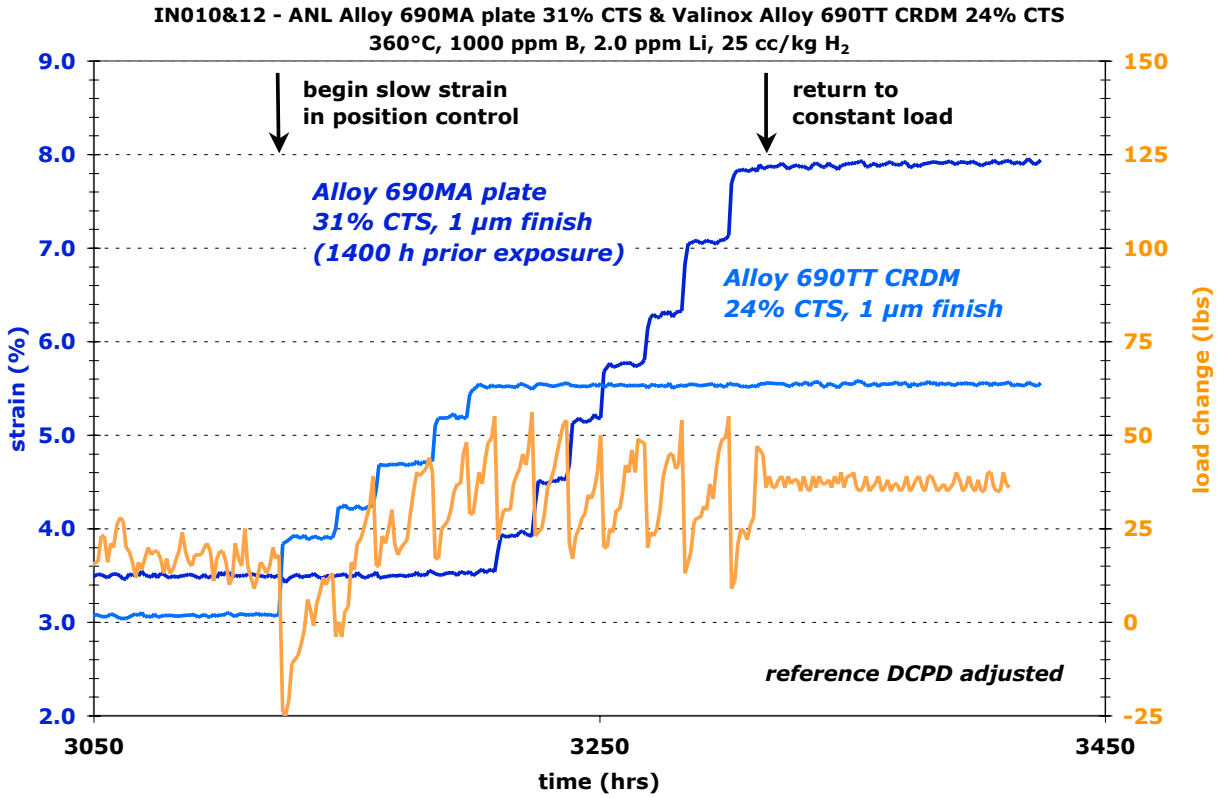

Figure 54. Slow straining response of the 31% tensile strained alloy 690 plate (IN010) combined with a 24% cold tensile strained alloy 690 CRDM specimen (IN012). Note that IN010 has 1400 hours of prior exposure.

Examinations have only been performed on the 31% tensile strained ANL alloy 690 plate specimen IN010 with Figures 55 and 56 showing a high density of slip bands intersecting the surface as well as cracks having nucleated from corroded TiN particles. Small TG cracks can be seen associated with many of the slip lines.

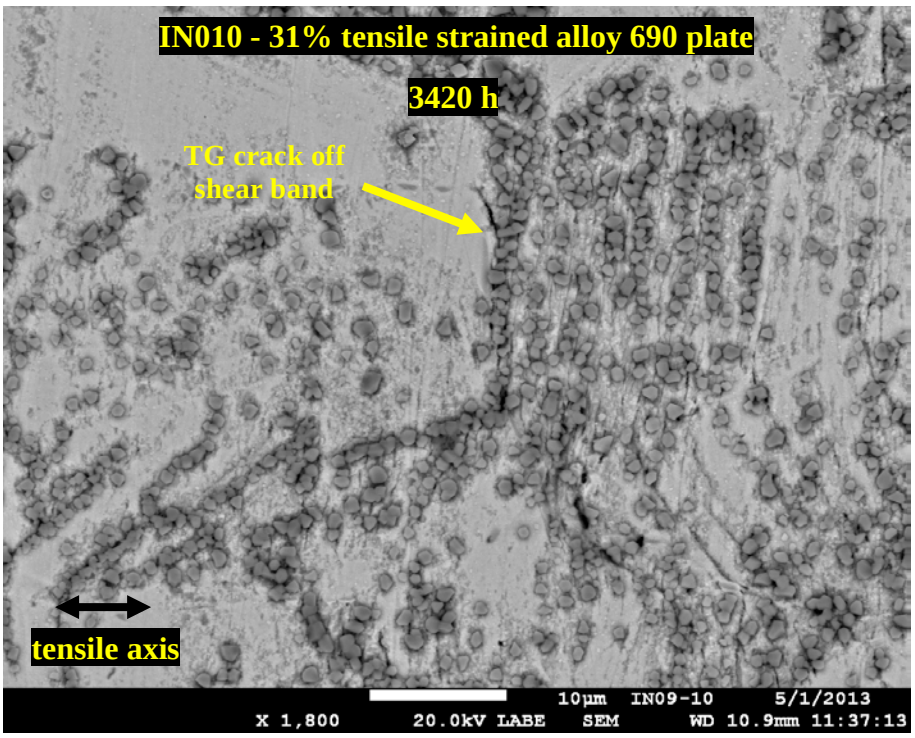

Figure 55. SEM-BSE image of the surface the 31% tensile strained ANL alloy 690 plate specimen (IN010) showing shear bands intersecting the surface. Crack appears to have formed at many shear bands. Large Ni-Fe spinels on the surface obscure the view.

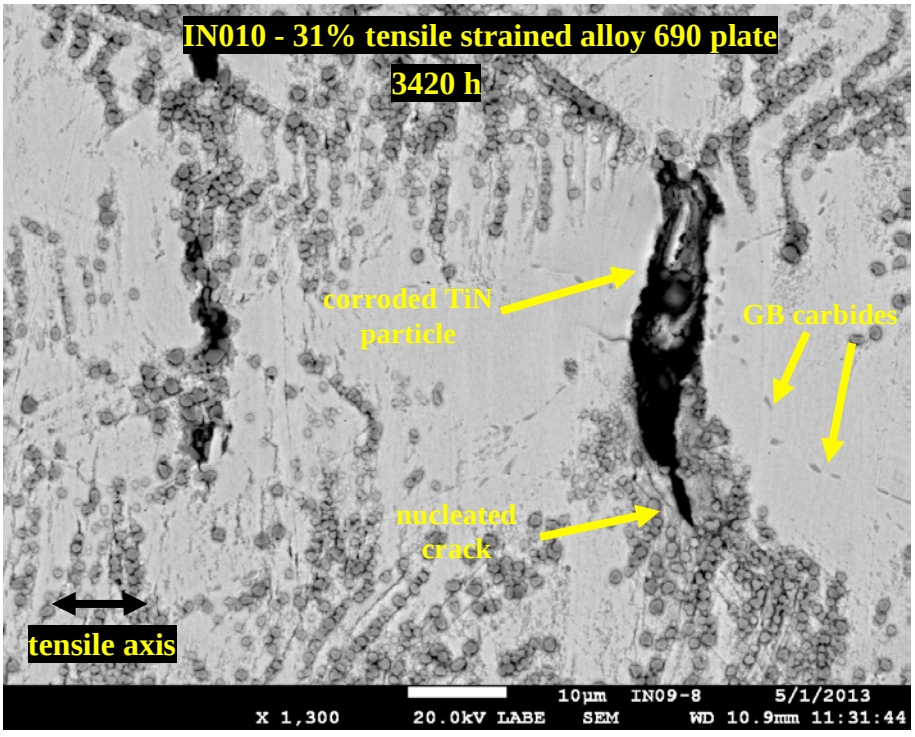

Figure 56. SEM-SE image of the surface the 31% tensile strained ANL alloy 690 plate specimen (IN010) showing shear bands intersecting the surface and cracks nucleated off of corroded TiN particles.

Discussion of Alloy 690 SCC Initiation Results

The approach for SCC initiation testing was established by our experiments on cold-worked alloy 600 [16] where crack nucleation was successfully detected within ~2500 hours. Even though it is clear that the mechanisms controlling corrosion and SCC are different for alloy 600 and alloy 690 in PWR primary water, cold-worked alloy 690 has been shown by many investigators to be highly susceptible to SCC crack growth. Moreover, SCC propagation rates comparable to those for mill-annealed alloy 600 have been measured for highly cold-worked alloy 690 materials. This similarity in SCC propagation rates led to an expectation that highly cold-worked alloy 690 would also be susceptible to SCC initiation in constant load tests.

The first phase of the SCC initiation test plan for alloy 690 was built around this hypothesis and utilized materials that exhibit high primary water SCC propagation rates (~$1x10^{-7}$ mm/s) when in a CR condition. SCC susceptible 26-31%CR materials (IN006/IN007) were selected to critically evaluate this assumption and begin investigations of key factors influencing SCC initiation in alloy 690. The lack of SCC initiation in these specimens after long exposures in 360°C simulated PWR primary water at high stresses modified expectations. While the total test time for the CR alloy 690 specimens is only 2-3x higher than the measured SCC initiation times for cold-worked alloy 600, surface characterizations on both stressed and unstressed alloy 690 revealed important differences in oxidation microstructures. A continuous chromia film forms above alloy 690 grain boundaries and effectively blocks IG corrosion/oxidation that acts as a precursor to SCC initiation in alloy 600. Results for the first constant load tests on SCC-susceptible alloy 690 specimens indicate that this protective chromia film is not broken down even after long exposures at the yield stress. Therefore, modifications to the testing approach were made to begin assessment of more aggressive dynamic strain effects.

Several different straining methods were explored in the phase 1 SCC initiation experiments. For the highly CR materials known to be susceptible to SCC growth, it was decided to periodically induce small amounts of in-situ tensile deformation at a moderate strain rate of ~$5x10^{-4}$ s^{-1}. The intent was to create surface damage and compromise the protective film leading to formation of SCC precursors. Most of this evaluation focused on the 26%CR ANL plate specimen IN006 when micrometer-length cracks were observed to nucleate off corroded TiN stringers that intersected the surface. Increasing plastic strain was found to increase the density and size of IG and TG cracks. However despite several applications of plastic strain and almost 4000 hours of additional exposure at very high stress, DCPD has yet to detect SCC initiation. The observation of the small IG surface cracks clearly indicates that IGSCC precursors have formed, but this SCC-susceptible alloy 690 remains remarkably resistant to additional growth under constant load conditions.

For another series of specimens that were cold tensile strained prior to SCC initiation testing, the effect of cyclic loading and slow strain rate extension were both assessed. While it was understood that cyclic loading up to yield stress would produce only elastic strains, it was hoped

that the strains would be sufficiently large to disrupt the surface oxide film. Although testing conditions were limited, no change in specimen response was observed during cyclic loading. The same specimens were then subjected to slow strain rate testing to ~3.5% plastic strain over a period of eight days (strain rate of ~$1x10^{-7}$ s^{-1}). This produced a high density of slip bands intersecting the surface with many having the appearance of cracks with lengths up to ~10 μm. These results are consistent with the slow strain rate testing of alloy 690 in 360°C PWR primary water by Moss [17]. Surface cracks of a similar length (average ~3 μm) were reported indicating that continuous dynamic strain can clearly lead to crack formation in alloy 690. An issue for the aggressive slow strain rate tests is whether they effectively assess SCC initiation response relevant to service components.

Phase 1 experimental results clearly demonstrate that alloy 690 materials can exhibit quite different susceptibility to SCC initiation versus SCC growth. Highly cold-worked alloy 690 that show very high SCC propagation rates in tests on compact tension specimens are remarkably resistant to SCC initiation in constant load tests on polished specimens. The parallel assessment of alloy 690 surface corrosion microstructures has shown that this material is resistant to IG corrosion/oxidation due to the formation of a protective chromia film above the grain boundaries intersecting the surface. As a result, SCC initiation from a smooth surface appears to be extremely difficult without aggressive straining to thin or break this protective oxide layer. It is interesting to note that strong Cr depletion is observed along grain boundaries to micrometer depths below the surface. Therefore if the protective layer is breached, IG corrosion and SCC of the Cr-depleted grain boundary might be expected. Preliminary results question this possibility since shallow IG cracks have been created after dynamic straining in the 26%CR ANL specimen IN006, yet there is no indication of significant IGSCC propagation. Much more detailed information will be available soon as the IN006/IN007 test is ended and more complete characterizations are performed.

An important conclusion from early experiments is that it may not be possible to determine differences in initiation response among alloy 690 variants and alloy 600 using constant load tests on smooth polished specimens. More aggressive plastic deformation appears to be required to nucleate cracks in alloy 690. The next phase of the experimentation at PNNL focuses on an improved understanding dynamic straining effects on grain boundary oxidation and crack initiation. Two key issues will be the production of IGSCC precursor structures and the conversion of these structures to growing SCC cracks. The first area will evaluate dynamic straining and stress concentration sites on IG crack nucleation. Tests have just started on cold-worked alloy 690 materials comparing the stress corrosion crack formation response during slow periodic straining of tensile specimens and blunt notch compact tension (CT) specimens. A key goal is to understand how stress, stress intensity and strain affect crack nucleation. In addition, the influence of surface damage and defects on SCC initiation is being assessed using identical cold-worked alloy 690 materials. Constant load along with periodic plastic straining will be employed to assess response of tensile and blunt notch specimens with ground surfaces

simulating weld preparation in plant. A final near-term research area will investigate the transition from short IG cracks to stable growing stress-corrosion cracks. SCC propagation rates are being evaluated at low stress intensities for these cold-worked alloy 690 materials to determine the threshold K dependence for SCC. These results will be directly compared to the blunt notch tests where critical crack depths for stable SCC growth will be measured.

Summary and Conclusions

SCC experimentation has revealed that cold worked alloy 690 is extremely resistant to SCC initiation even though it is highly susceptible to SCC growth. The first attempts to produce SCC initiation in constant load tests at high stress, a method observed to be very effective in alloy 600, did not produce SCC despite the formation of small TG and IG cracks into the matrix from corroded TiN intersecting the surface. Efforts to accelerate the crack initiation process by various methods, including plastic straining, have produced more significant surface cracking, but no evidence of SCC. The nucleated surface cracks remain in the micrometer size range and have not yet transitioned to SCC growth. Detailed microstructural investigations of alloy 690 materials exposed to PWR primary water have revealed that a protective chromia layer forms above grain boundaries and this film appears to remain protective during constant load testing at high stresses. Significant grain boundary chromium depletion is detected for several micrometers below the surface that may promote IG oxidation and SCC if the chromia film is breached. However, small IG cracks have been produced during SCC testing without any evidence for preferential grain boundary oxidation or a transition to IGSCC growth. Experiments and high-resolution characterizations are continuing to elucidate mechanisms of SCC initiation in alloy 690 and determine how microstructural and mechanical processes influence crack nucleation.

Acknowledgments

The authors would like to recognize the collaborative funding from the Office of Basic Energy Sciences for APT characterizations, the Nuclear Regulatory Commission for SCC crack growth tests on alloy 690 materials and Rolls Royce & Associates for detailed examinations on cold-worked microstructures. These collaborations have been essential to the success of the SCC research. Critical technical assistance is also recognized from Rob Seffens, Anthony Guzman and Clyde Chamberlin.

References

1. S. M. Bruemmer and M. B. Toloczko, *Pacific Northwest National Laboratory Investigation of Stress Corrosion Cracking in Nickel-Base Alloys*, NUREG/CR-7103, Volume 2, Nuclear Regulatory Commission, Office of Nuclear Regulatory Research, November 2011.

2. S. M. Bruemmer, M. J. Olszta, M. B. Toloczko and L. E. Thomas, *High-Resolution Characterizations of Grain Boundary Damage and Stress Corrosion Cracks in Cold-Rolled Alloy 690*, Proc. 15th International Conference on Environmental Degradation of Materials in Nuclear Power Systems-Water Reactors, The Minerals, Metals and Materials Society, 2012.

3. D. S. Morton, et. al., *SCC Initiation Testing of Nickel-Base Alloys in High Temperature Water,* Proc. 14th International Conference on Environmental Degradation of Materials in Nuclear Power Systems-Water Reactors, American Nuclear Society, 2009.

4. M. J. Olszta, D. K. Schreiber, L. E. Thomas and S. M. Bruemmer, *Penetrative Internal Oxidation from Alloy 690 Surfaces and Stress Corrosion Crack Walls during Exposure to PWR Primary Water*, Proc. 15th International Conference on Environmental Degradation of Materials in Nuclear Power Systems-Water Reactors, The Minerals, Metals and Materials Society, 2012.

5. M. J. Olszta, D. K. Schreiber, M. B. Toloczko and S. M. Bruemmer, *Alloy 690 Surface Nanostructures During Exposure to PWR Primary Water and Potential Influence on Stress Corrosion Crack Initiation,* Proc. 16th International Conference on Environmental Degradation of Materials in Nuclear Power Systems-Water Reactors, NACE International, 2013, in press.

6. A. Machet, et al., *XPS study of oxides formed on nickel-base alloys in high-temperature and high-pressure water,* Surface and Interface Analysis, **34**(1), 2002, p. 197-200.

7. X. Y. Zhong, E.H. Han, and X.Q. Wu, *Corrosion behavior of Alloy 690 in aerated supercritical water,* Corrosion Science, **66**, 2013, p. 369-379.

8. H. Lefaix-Jeuland, et al., *Oxidation kinetics and mechanisms of Ni-base alloys in pressurised water reactor primary conditions: Influence of subsurface defects.* Corrosion Science, **53**(12), 2013, p. 3914-3922.

9. F. Carrette, *Analysis and TEM examination of corrosion scales grown on Alloy 690 exposed to pressurized water at 325 degrees C,* Surface and Interface Analysis, **34**(1), 2002, p. 135-138.

10. M. Sennour, et al., *A detailed TEM and SEM study of Ni-base alloys oxide scales formed in primary conditions of pressurized water reactor.* Journal of Nuclear Materials, 2010. **402**(2-3): p. 147-156.

11. M. J. Olszta, D. K. Schreiber, L. E. Thomas and S. M. Bruemmer, *Penetrative Internal Oxidation from Alloy 690 Surfaces and Stress Corrosion Crack Walls during Exposure to PWR Primary Water*. in *Proceedings of the 15th International Conference on Environmental Degradation of Materials in Nuclear Power Systems-Water Reactors*. 2012. John Wiley and Sons, Inc.

12. F. Carrette, et al., *Analysis and TEM examinations of corrosion scales grown on alloy 690 exposed to PWR environment.* Materials at High Temperatures, 2003. **20**(4): p. 581-591.

13. F. Delabrouille, et al., *Effect of the chromium content and strain on the corrosoin of nickel based alloys in primary water of pressurized water reactors,* Proc. 12th International Conference on Environmental Degradation of Materials in Nuclear Power Systems-Water Reactors, 2005, John Wiley and Sons, Inc.

14. P. Combrade, et al., Oxidation of Ni Base Alloys in PWR Water: Oxide Layers and Associated Damage to the Base Layer, Proc. 12th International Conference on Environmental Degradation of Materials in Nuclear Power Systems-Water Reactors, 2005, John Wiley and Sons, Inc.

15. J. Panter, et al., *Influence of oxide films on primary water stress corrosion cracking initiation of alloy 600.* Journal of Nuclear Materials, 2006. **348**(1-2): p. 213-221.

16. M. B. Toloczko, M. J. Olszta, D. K. Schreiber and S. M. Bruemmer, *Stress Corrosion Crack Initiation of Alloy 600 in PWR Primary Water Environments,* Technical Milestone Report, Light Water Reactor Sustainability Program, DOE Office of Nuclear Energy, March 2013.